

Surface Phenomena of Semiconductor Materials:  
An Investigation using Raman Microscopy

(顕微ラマン分光法を用いた半導体材料の界面現象に  
関する研究)

Katsuhiro AJITO

0

**Surface Phenomena of Semiconductor Materials:  
An Investigation using Raman Microscopy**

(顕微ラマン分光法を用いた半導体材料の界面現象に関する研究)

**Katsuhiro AJITO  
(1995)**

**Department of Applied Chemistry  
Faculty of Engineering  
The University of Tokyo**

## CONTENTS

1. INTRODUCTION	1
1.1. General Introduction	1
1.2. Fundamental Technologies used in New Micro-Raman System	3
Raman Spectroscopy	
Raman Microscopy	
1.3. Advantages of New Micro-Raman System	6
Overview of Advantages of New Micro-Raman System	
Advantage 1. High Sensitivity	
Advantage 2. Raman Imaging	
Introduction	
a) Automated Point-by-Point Mapping	
b) Direct Filter Imaging	
Advantage 3. Electrochemical Measurements	
Advantage 4. Combined Raman-Photoelectrochemical Imaging	
Advantage 5. Imaging of Peak Width and Peak Position	

References

2.	DESCRIPTION OF NEW MICRO-RAMAN SYSTEM INSTRUMENTATION	18
2.1.	Overview of New Micro-Raman System	18
2.2.	Subsystem 1. A commercialized Raman Microscope with Direct Filter-Imaging System	18
2.3.	Subsystem 2. Electrochemical System	20
2.4.	Subsystem 3. Point-by-Point Raman Imaging System	20
2.5.	Subsystem 4. Photocurrent Imaging System	21
2.6.	Subsystem 5. Computer and Software	22
	References	

3.	APPLICATIONS INVOLVING SURFACE PHENOMENA OF SEMICONDUCTORS USING NEW MICRO-RAMAN SYSTEM	28
3.1	Introduction	28
3.2.	Example 1. A Study of the Photochromic Properties of Amorphous MoO <sub>3</sub> Films Using Raman Microscopy	30
	Introduction	
	Experimental	
	Results	
	Discussion	
	Conclusions	
	References	

3.3. Example 2. Raman Imaging Analysis of Microscale Crystallization of MoO<sub>3</sub> Thin Films

54

Introduction

Experimental

Results and Discussion

Summary

References

3.4 Example 3. Combined Raman and Photoelectrochemical Imaging System. Application to TiO<sub>2</sub> Films Grown Anodically on Ti-Ag Alloy

62

Introduction

Experimental

Results and Discussion

Summary

References

3.5 Example 4. Strain Imaging Analysis of Si Using Raman Microscopy

73

Introduction

Experimental

Results

Discussion

Conclusions

References

#### 4. SUMMARY AND FURTHER MICRO-RAMAN SPECTROSCOPIC APPLICATIONS

88

References

PUBLICATION LIST

PRESENTATION LIST

ACKNOWLEDGMENTS

# INTRODUCTION

## 1.1. General Introduction

The technological importance of the surfaces of semiconductor and metal oxide materials is evident in various areas such as photocatalysis, corrosion, chemical sensors and batteries. In all of these areas, characterization of the surface is critical for the understanding of processes such as charge transport at the interface, and damage and/or strain at the surface, as well as for the preparation of new materials designed for specific applications.

Vibrational spectroscopy, i. e., infrared and Raman, can provide nondestructive and quantitative microanalysis of semiconductor surface structures and their electrical properties. Raman microprobe spectroscopy has particularly high spatial ( $1\ \mu\text{m}$ ) and spectral ( $0.1\text{--}1\ \text{cm}^{-1}$ ) resolution and can easily be applied in aqueous solution systems, e.g., semiconductor electrode/electrolyte interfaces. However, low sensitivity has been a problem, and consequently its use has been limited. Recently, several fundamental optical techniques were developed, such as holographic laser rejection filters, high-throughput monochromators or band-pass filters, and highly sensitive charge-coupled device (CCD) cameras. These techniques are very useful in increasing the sensitivity of Raman measurements, which has made possible Raman measurements of semiconductors using relatively low power lasers and short data acquisition times.

The purposes of this study were 1) to develop a new high sensitivity micro-Raman system using the above techniques, e.g., an electrochemical micro-Raman system, a micro-Raman imaging system, and a combined Raman-photoelectrochemical imaging system, and 2) to demonstrate the performance of these systems in the study of surface phenomena of semiconductor and metal oxide materials.

At the same time that the author was searching for state-of-the-art equipment with which to develop a new micro-Raman system, a new type of commercial micro-Raman spectrometer was reported, which combined holographic laser rejection filters, high-throughput monochromators or band-pass filters, and highly sensitive CCD cameras. The author decided to modify this type of spectrometer to develop a high sensitivity micro-Raman system for the characterization of semiconductor and metal oxide surfaces.

The fundamental technologies which were used in the new micro-Raman system, i.e., Raman spectroscopy and particularly Raman microscopy, are described in Section 1.2. Section 1.3, the final section of Chapter 1, discusses the five advantages of the new micro-Raman system, i.e., 1) high sensitivity, 2) Raman imaging, 3) electrochemical measurements, 4) combined Raman-photoelectrochemical imaging, and 5) imaging of peak width and peak position.

Chapter 2 provides further details on the new micro-Raman system, which was constructed from five subsystems, i.e., 1) a commercial Raman microscope with direct filter-imaging system, 2) electrochemical system, 3) automated point-by-point Raman mapping system, 4) photocurrent imaging system, and 5) computer and software.

Four applications involving surface phenomena of semiconductors using the new micro-Raman system are described in Chapter 3, including 1) photochromic properties of  $\text{MoO}_3$  films, 2) imaging analysis of microscale crystallization of  $\text{MoO}_3$  films, 3) combined Raman-photoelectrochemical imaging analysis of  $\text{TiO}_2$  films, and 4) strain imaging analysis between  $\text{Si/SiO}_2$  interfaces.

Finally, in Chapter 4, the results of the present thesis are summarized, and future prospects for micro-Raman spectroscopy for the study of surface phenomena of semiconductor materials are discussed.

## 1.2. Fundamental Technologies used in New Micro-Raman System

### Raman Spectroscopy<sup>1-3</sup>

The Raman effect was first observed in 1928 by C. V. Raman<sup>4</sup>; however, it has not been until the relatively recent development of lasers in the 1960s that the method has become more widely applied to a variety of problems. Initially, the Raman method was used to analyze large volume samples with a macro-sampling configuration. Only in the past 20 years has it been applied to the analysis of much smaller, micron-sized samples using optical microscopes interfaced to excitation spectrometer systems. Before getting into the advantages of Raman spectroscopy, an introduction to Raman scattering is described.

Unlike absorption spectroscopy, Raman scattering involves a change in photon frequency. When light encounters the surface of a semiconductor, most is reflected, transmitted, or Rayleigh-scattered because of first-order elastic interactions with electrons, phonons, and impurities. There is no change in photon frequency. But a small part of the light interacts inelastically with phonon modes, producing outgoing photons whose frequencies are shifted from the incoming values. These are the Raman-scattered photons. They gain energy by absorbing a phonon (anti-Stokes-shifted), or lose energy by emitting one (Stokes-shifted), according to the energy and momentum conservation rules:

$$\omega_s = \omega_i \pm \Omega \quad (1.1)$$

$$\mathbf{q}_s = \mathbf{q}_i \pm \mathbf{K} \quad (1.2)$$

where  $\omega_i$  and  $\omega_s$  are the incoming and scattered photon frequencies respectively,  $\mathbf{q}_i$  and  $\mathbf{q}_s$  are incoming and scattered photon wavevectors, respectively, and  $\Omega$  and  $\mathbf{K}$  are the phonon frequency and wavevectors respectively. Raman scattering is inherently a weak process and lasers are necessary to obtain Raman spectra.

Raman spectroscopy as an analytical tool offers the user certain advantages over other routine methods of analysis. It is a light-scattering method of analysis, which means that it is non-intrusive and that the sample size is not a restriction for the analysis. In addition, because visible laser wavelengths are routinely used to stimulate Raman scattering, conventional glass optics, lenses and windows are fully transmissive and can be used without any reduction in sensitivity. As a consequence, the design of *in situ* cells for dynamic spectroscopic analysis is straight forward. Basically, if a laser beam can be focused on a sample, be it a micron-sized particle (using an optical microscope) or a large column of chemical reactants held in a high pressure reaction flask, a successful analysis can be achieved. The advantage of using glass optics in a Raman experiment can be further extended to make use of fiber optics to achieve remote sampling away from the instrumentation. This application has been demonstrated by a variety of groups who have been able to show good sensitivity up to 100 m away from the spectrometer.<sup>5</sup>

One of the major drawbacks of infrared spectroscopy has been the problems associated with recording spectra from aqueous phase media. This is due to the very strong infrared absorptions in the O-H region of the spectrum. However, owing to the complementary nature of infrared and Raman spectroscopy and the different selection rules that apply, it is often the case that bands which are strong in the Raman are weak in the infrared and vice versa. This leads to very weak water bands being observed in the Raman spectrum, thus making it an ideal solvent for the method.

### **Raman Microscopy<sup>2,6-9</sup>**

Raman microscopy was first demonstrated in 1975.<sup>10</sup> This was achieved by the simple interfacing of an optical microscope with an excitation spectrometer. Before describing the technique in detail of the system, some of the advantages and also some of the limitations, in general, must be noted. One advantage, is the ability to observe

samples, not under vacuum, but in air or under a controlled atmosphere or even immersed in a liquid. The main limitation of the method arise from the inherent weakness of the Raman effect. We must note in particular that

(i) The scattering of the *parent (Rayleigh) line* by all components of the instrument has to be reduced to the lowest possible level, and careful attention must be paid to the optical choice of the optimal system in order to avoid stray light.

(ii) Unfortunately the use of the use of powerful lasers to increase the Raman intensity is forbidden for microsamples, because *local heating* created by absorption of the laser beam may cause decomposition of the sample.

(iii) *Fluorescence* emitted by the sample may make the detection of Raman scattering difficult.

Raman instrumentation for micro-sampling has been commercially available virtually since the first demonstration of the method. This was achieved by simply taking a conventional optical microscope together with transfer optics and interfacing to a spectrometer entrance port on a double- or triple-Raman spectrometer. The interfacing of the microscope to a spectrometer is shown in Fig. 1.2.1. This design has been little changed over the years and is still used in most conventional instruments. It provides an excellent spatial resolution of 1  $\mu\text{m}$ . However, the use of a beamsplitter in the optical path (usually 50/50 or 70/30) reduces the overall efficiency of the system, resulting in the use of high power lasers and less than optimum collection of the Raman signal. In addition, the use of a pinhole, which acts as a spatial filter, dramatically reduces the overall efficiency. This is placed at the back focal plane of the microscope to limit the amount of unwanted scatter from outside the focus of the laser spot on the sample passing into the spectrometer. However, the presence of the pinhole does ensure a good confocal arrangement providing spatial resolution as a function of sample depth.

Until very recently the overall efficiency of the detection of Raman photons has been relatively poor. Raman instruments, with microscopes, have been based around double and triple spectrometers which, by their nature contain a large number of optical

surfaces and are relatively inefficient. The conventional detectors used with Raman systems have been either a multichannel intensified diode array or a single-channel photomultiplier tube. Spectra have taken some minutes and often hours to acquire using these detectors.

### 1.3. Advantages of New Micro-Raman System

#### Overview of Advantages of New Micro-Raman System

The new micro-Raman system developed in this work provides four advantages for the characterization of semiconductor surfaces, i.e., 1) *high sensitivity*, 2) *Raman imaging*, 3) electrochemical measurements, 4) combined Raman–photoelectrochemical imaging, and 5) imaging of peak widths and peak positions. The first advantage, *high sensitivity*, which is the most basic and important in these advantages, can lead to the use of relatively low-power lasers and short data acquisition times. On the other hand, combining a relatively short acquisition time (ca. 1 ms ~ 1 s) with an automated mapping stage provides second advantage, point-by-point Raman *imaging* microscopic analysis, which is very useful for the study of the surface characteristics of heterogeneous semiconductor and metal oxide materials. The third advantage, electrochemical measurements, is a necessary subsystem for the study of semiconductor electrode/electrolyte interfaces. As described in Section 1.2, Raman measurements which use visible laser wavelengths are easy to apply in a variety of aqueous solutions held by a glass cell and/or a glass window which are fully transmissive. The fourth advantage, combined Raman–photocurrent imaging, which is a very unique technique, provides a two-dimensional relationship between structural information and photocurrent and/or photovoltage at the surface of semiconductor materials. The final advantage, imaging of peak width and peak position is supported by an automated curve-fitting program. As

well as Raman intensity, peak width and peak position, which show the degree of damage and strain respectively, provide more detailed two-dimensional structural information at the surface of semiconductor materials. The details of each of these advantages are described in the next several sections.

### **Advantage 1. High Sensitivity**

Over the past five years, two other major advances which have had a large impact on Raman spectroscopy were taking place. First, the CCD camera, developed and used extensively by astronomers, became acknowledged as a real advance for the Raman spectroscopist. This two-dimensional silicon array detector has the properties of high quantum efficiencies (up to 70% for back-thinned devices) and extremely low dark current levels (typically  $< 0.001 e^- \text{ pixel}^{-1} \text{ s}^{-1}$ ), which is far improved over the conventional photomultiplier and intensified photodiode array technology.<sup>11</sup> In addition to the enhanced performance capability, the CCD detector also offers the capability of being utilized as a two dimensional array to provide both spectral and spatial information simultaneously.

The second major advance in Raman spectroscopy in recent years has been the advent of the Raman holographic filter. These filters are wavelength specific and possess the property of efficiently blocking the undesirable Rayleigh-scattered light in a Raman experiment, with an optical density of ca. 4, and a cut-off that routinely permits approach to within  $100 \text{ cm}^{-1}$  of the laser line. This advance has meant that the Raman experiment, which has historically used high-dispersion double or triple monochromators to filter out the elastically scattered laser radiation, can be conveniently performed with a simple single spectrograph together with a Raman holographic filter.<sup>12</sup> This approach to Raman spectroscopy provide considerable benefits. The expense involved in purchasing such a system is relatively low and its operation can be rendered more routine. The throughput

efficiency of a single-grating system is far higher than, for example, a triple monochromator. When a single-spectrograph-based Raman system is coupled to a CCD detector, it provides much higher sensitivity levels, which can lead to the use of low power lasers and shortened data acquisition times. A typical schematic of a micro-Raman system is shown in Fig. 1.3.1a. The efficient coupling of a microscope to such a system presents no real difficulties, with the spot size emerging from the microscope being compatible with the narrow slit widths used in dispersive Raman systems. Recent publications have detailed many of these advantages and discussed the merits of this approach over the FT-Raman method.<sup>12</sup> The increased levels of sensitivity coupled with similar discrimination over fluorescence when using near-infrared diode laser wavelengths, between 750 and 830 nm,<sup>13</sup> make the more traditional approach to Raman spectroscopy very attractive.

## **Advantage 2. Raman Imaging**

### **Introduction**

Raman imaging has been approached in several different ways. Delhaye and Dhamelincourt<sup>8</sup> developed three types of Raman imaging shown in Fig. 1.3.2. In the *first microprobe*, the laser beam is focused to approach the diffraction limit and the spot is rapidly deflected to scan a line on the sample area. During scanning an efficient lens with a very large aperture collects the scattered light and focuses it on the slit of a monochromator pre-set at a fixed wavelength corresponding to the desired Raman line. A single channel detector is employed (i.e., a photomultiplier tube), the output of which is amplified, filtered with the proper bandwidth and displayed on an oscilloscope by means of a television-type scanning system synchronized with the exploration of the sample.

In the *second microprobe*, by making use of a multichannel detector (an image intensifier tube and an electronic camera) a large number of points may be simultaneously analyzed. Several hundred points along a straight line may easily be simultaneously focused on the slit of the monochromator and analyzed. This system enables advantage to be taken of the 'multichannel technique' provided that the monochromator possesses *stigmatic properties*. The image mapping is obtained by a frame-scanning movement of the examined object.

In the *third experimental arrangement*, the whole area of the object is continuously illuminated by the unfocused laser radiation. An integral image of the area is observed through an optical filter which isolates the chosen Raman radiation. The characteristics of the image obtained (i.e., the resolving power) are similar to those of images formed by a conventional optical microscope. These authors developed this type of system and constructed a Laser Raman Molecular Microprobe (MOLE) which used a double concave holographic grating filter and TV camera.<sup>9</sup>

However, in order to maintain the resolving power of the microscope objective over the whole optical system, the slit-width of the monochromator must be as wide as the projection of the exit pupil of the microscope objective, i.e., typically a few millimeters in diameter. Therefore, the MOLE microprobe suffers from poor light rejection, low resolution performance and also a lack of sensitivity that limits the applications to a small number of samples consisting of fluorescence-free strong Raman scatters.

The new micro-Raman system, which the author developed, including two types of imaging techniques, i.e., a) automated point-by-point mapping and b) direct filter imaging. These techniques are similar to the experimental arrangements shown in Figs. 1.3.2a and 1.3.2c, respectively developed by Delhaye and Dhameincourt; however, several new techniques are used in order to increase the sensitivity and to expand the utility for Raman imaging. Both types of imaging techniques have the ability to obtain high sensitivity, described in the prior section, Advantage 1, and a high spatial resolution

( $\sim 1 \mu\text{m}$ ), but advantages are depend out on measurement conditions. More details are described in the next two sections.

#### **a) Automated Point-by-point Mapping**

The concept of this method is very similar to the system shown in Fig. 1.3.2a, but the sensitivity is much increased. This imaging method has two advantages. The first advantage is the possibility of measuring many Raman bands simultaneously by a using CCD multichannel detector, which provides detection, identification, and distribution of different components in heterogeneous samples. This type of technique was developed by Bowden and coworkers,<sup>14</sup> and their system, including a stepper-motor-driven XY stage and an image processor, was controlled by a computer instead of an oscilloscope, which Delhaye and Dhamelin court used. However, the sensitivity of their system was probably lower than that of our system, because they used a simple triple monochromator and an intensified diode array detector.

The second advantage is to be able to measure a large scanning area. The maximum size of the scanning area of our system is about  $20 \times 20 \text{ mm}$ . Furthermore, the third advantage is that modification or combination with other laser scanning techniques are very easy because the optical paths are very simple.

#### **b) Direct Filter Imaging**

The schematic of this technique is shown in Fig. 1.3.1b. The concept of this method is very similar to the system shown in Fig. 1.3.2c, but the sensitivity is much increased. The advantage of this method is very clear, i.e., a short acquisition time (ca. 1 s $\sim$ 1 min.). The laser spot size used to illuminate the sample is de-focused from  $1 \mu\text{m}$  to  $200 \mu\text{m}$  diameter. The systems consist of a microscope, a holographic notch filter to eliminate the exciting radiation, either a set of interference filters or a tunable acoust-optic

filter (ATOF) to isolate a characteristic Raman band, and a high-sensitivity low-noise CCD detector. (The high performance of combined a holographic notch filter and a high-sensitivity low-noise CCD detector for a Raman spectrum single point is mentioned for Advantage 1 in Section 1.3) An interference filter-type Raman imaging system was described by Williams et al.,<sup>2,7</sup> and many types of applications were reported by Batchelder et al., e.g. Langmuir-Blodgett films,<sup>15</sup> GaAs micrometer-sized dots,<sup>16</sup> polymer blends,<sup>17</sup> and diamond films.<sup>18</sup> On the other hand, an ATOF-type Raman imaging system was described by Treado et al.<sup>19</sup>

### **Advantage 3. Electrochemical Measurement**

The new Micro-Raman system includes a normal three-electrode electrochemical system, which provides the possibility for a variety of *in situ* measurements of semiconductor electrode/electrolyte interfaces, e.g., photoelectrochemical measurements described in the next section. The description of the electrochemical system is described in Section 2.3 of Chapter 2.

### **Advantage 4. Combined Raman-Photoelectrochemical Imaging**

In recent years an impressive array of analytical techniques has been utilized to investigate the properties of anodic films formed on metal surfaces. A key factor in studying these oxide films is the ability to conduct the investigation *in situ* and avoid the complications associated with *ex situ* techniques such as possible changes in the film structure. Two *in-situ* methods that have been commonly used in the study of oxide films are Raman spectroscopy and photoelectrochemical measurements, i.e., photocurrent (or photovoltage) measurements. The schematic models of physical processes of these methods are shown in Fig. 1.3.3. In order to better understand the properties of these films, the author developed a system combining Raman and

photoelectrochemical imaging measurements. The advantage of this system is to compare directly the *in situ* Raman and photocurrent- or photovoltage mapped images over the same area. The instrumentation is described in Section 2.5 of Chapter 2.

#### **Advantage 5. Imaging of Peak Width and Peak Position**

The images which are generated from peak widths and peak positions are calculated by an automated curve-fitting program. In addition to peak intensities, the linewidth (or peak width) and band frequency (or peak positions) are also main Raman parameters which can be used to characterize the lattice, impurities, and free carriers in a semiconductor. The linewidth shows the lifetime of a phonon. When a material is damaged or disordered, the linewidth increases, because these conditions increase phonon damping or change the rules for momentum conservation in the Raman process. The band frequency shifts of Raman phonon bands are related to changes in the force constants of the bond, which also can determine the degree of stress in materials such as Si, Ge, GaAs, GaSb, and ZnSe.<sup>20,21</sup> Furthermore, the frequencies of the longitudinal plasmon modes give the carrier density. However, the calculation of the peak widths and peak positions in a whole image (ca. 10,000–40,000 points) is not easy and requires automated software and a fast computer. This method is the first attempt and showed have a big impact in the area of Raman imaging techniques.

#### **References**

- 1 S. Perkowitz, *Optical Characterization of Semiconductors: Infrared, Raman, and Photoluminescence Spectroscopy* (Academic Press, London, 1993).
- 2 K. P. J. Williams and D. N. Batchelder, *Spectrosc. Eur.* **6**, 19 (1994).
- 3 J. R. Ferraro and K. Nakamoto, *Introductory Raman Spectroscopy* (Academic Press, Boston, 1993).

- 4 C. V. Raman, *Indian J. Phys.* **2**, 1 (1928).
- 5 M. L. Myrick and S. M. Angel, *Appl. Spectrosc.* **44**, 565 (1990).
- 6 K. P. J. Williams, G. D. Pitt, D. N. Batchelder, and B. J. Kip, *Appl. Spectrosc.* **48**, 232 (1994).
- 7 K. P. J. Williams, G. D. Pitt, B. J. E. Smith, A. Whitley, D. N. Batchelder, and I. P. Hayward, *J. Raman Spectrosc.* **25**, 131 (1994).
- 8 M. Delhaye and P. Dhamelincourt, *J. Raman Spectrosc.* **3**, 33 (1975).
- 9 P. Dhamelincourt, F. Wallart, M. Leclercq, A. T. N'Guyen, and D. O. Landon, *Anal. Chem.* **51**, 414A (1979).
- 10 G. J. Rosasco, E. Roedder, and J. H. Simmons, *Science* **190**, 5557 (1975).
- 11 C. A. Murray and S. B. Dierker, *J. Opt. Soc. Am.* **A3**, 2151 (1986).
- 12 S. M. Mason, N. Conroy, M. N. Dixon, and K. P. J. Williams, *Spectrochim. Acta, Part A* **49**, 633 (1993).
- 13 N. S. Ferris and R. B. Bilhorn, *Spectrochim. Acta, Part A* **47**, 1149 (1991).
- 14 M. Bowden, G. D. Dickson, D. J. Gardiner, and D. J. WOOD, *Appl. Spectrosc.* **44**, 1679 (1990).
- 15 R. V. Sudiwala, C. Cheng, E. G. Wilson, and D. N. Batchelder, *Thin Solid Films* **210/211**, 452 (1992).
- 16 P. D. Wang, C. Cheng, C. M. S. Torres, and D. N. Batchelder, *J. Appl. Phys.* **74**, 5907 (1993).
- 17 A. Garton, D. N. Batchelder, and C. Cheng, *Appl. Spectrosc.* **47**, 922 (1993).
- 18 I. P. Hayward, K. J. Baldwin, D. M. Hunter, D. N. Batchelder, and G. D. Pitt, *Diamond Relat. Mater.* **4**, 617 (1995).
- 19 P. J. Treado and M. D. Morris, *Appl. Spectrosc.* **44**, 1 (1990).
- 20 F. Cerdeira, C. J. Buchenaur, F. H. Pollark, and M. Cardona, *Phys. Rev.* **B5**, 580 (1972).
- 21 E. Anastasskis, A. Pinczuk, E. Burstein, F. H. Pollak, and M. Cardona, *Solid State Commun.* **8**, 133 (1970).

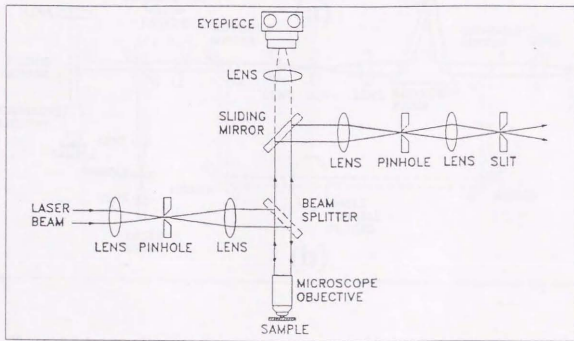


Figure 1.2.1. A schematic optical layout for the interfacing of the Raman microscope with the spectrometer, illumination and collection optics (ref. 2).

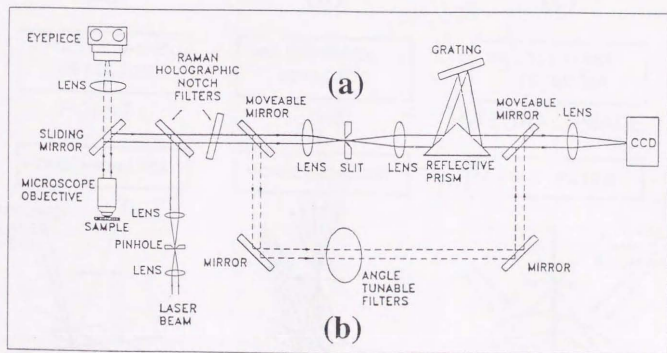


Figure 1.3.1. A schematic diagram of a new high sensitivity Raman spectrometer, including (a) spectroscopic and (b) two-dimensional direct filter-imaging measurement systems (ref. 2).

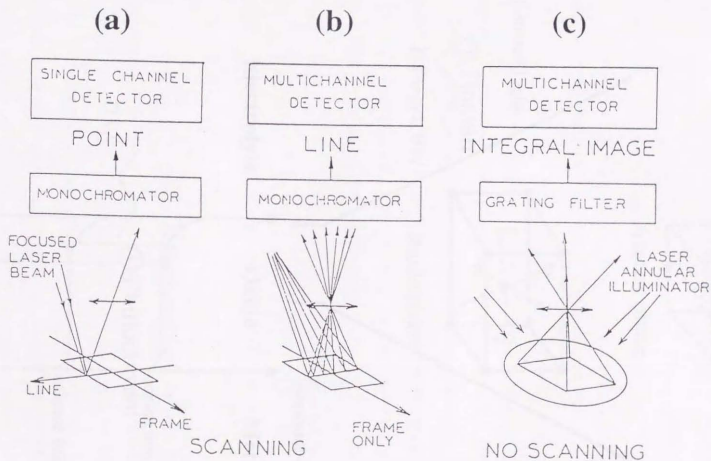


Figure 1.3.2. Schematic representations of the methods for obtaining images of samples with characteristic Raman frequencies: (a) Point-by-point mapping system; (b) Frame-scan mapping system; and (c) Direct filter-imaging system (ref. 8).

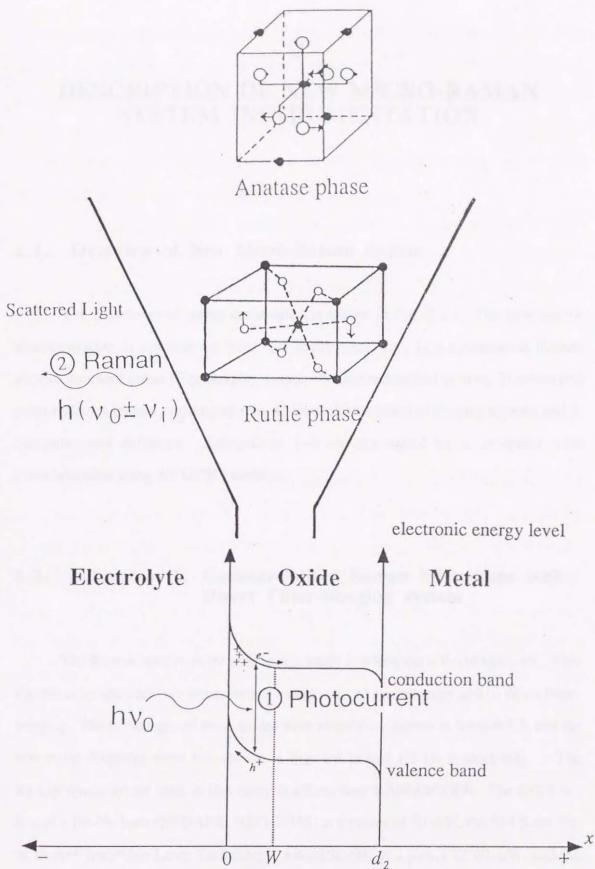


Figure 1.3.3. Schematic models of the physical processes of 1) photocurrent and 2) Raman spectral measurements. As a typical example, the two crystal phases of  $\text{TiO}_2$ , i.e., anatase and rutile, are shown.

## DESCRIPTION OF NEW MICRO-RAMAN SYSTEM INSTRUMENTATION

### 2.1. Overview of New Micro-Raman System

The experimental set-up constructed is shown in Fig. 2.1.1. The new micro-Raman system is constructed from five subsystems, i.e., 1) a commercial Raman microscope with direct filter imaging system, 2) electrochemical system, 3) automated point-by-point Raman mapping system, 4) photoelectrochemical imaging system, and 5) computer and software. Subsystems 1-4 are controlled by a computer with communication using AT-GPIB interfaces.

### 2.2. Subsystem 1. Commercialized Raman Microscope with Direct Filter-Imaging system

The Raman spectrometer used in this study is a Renishaw RAMASCOPE. This spectrometer includes two measurement modes, i.e., a) spectroscopy and b) direct filter-imaging. The advantages of these modes were already mentioned in Section 1.3, and the schematic diagrams were also shown in Fig. 1.3.1a and 1.3.1b, respectively. The Raman spectrometer used in this study is a Renishaw RAMASCOPE. The 632.8 nm line of a He-Ne laser (NEOARK, NEO-30MS) at a power of 30 mW, the 514.5 nm line of an Ar<sup>+</sup> laser (Ion Laser Technology, 5490ASL-00) at a power of 40 mW, and the 514.5 nm line of an Ar<sup>+</sup> laser (Coherent, Enterprise 622) at a power of 100 mW, are

used as the excitation light sources. The optical paths of these lasers are selected using mirrors. Two objective lenses (40 $\times$ , 4 $\times$ ), located outside the microscope, are used in conjunction with a pinhole having a diameter of 10  $\mu\text{m}$  to expand the laser spot size. The light is then focused onto the sample using 100 $\times$ , 50 $\times$ , 20 $\times$ , 10 $\times$  and 5 $\times$  objective lenses mounted on an Olympus BH-2 optical microscope. The size of the laser spot is  $\sim 1 \mu\text{m}$  for the 100 $\times$  and  $\sim 2 \mu\text{m}$  for the 50 $\times$  objective lenses, respectively.

The Raman spectrometer is physically connected to the optical microscope to record the Raman spectrum. The same objective lens used to focus the laser onto the sample is used to collect light reflected from the sample at 180 $^\circ$  with respect to the incident light. After passing through a holographic notch filter, which removes the Rayleigh line component, the scattered light is focused onto the entrance slit of a monochromator for the spectroscopic mode (a). A 1/4-meter single monochromator fitted with 1800 grooves  $\text{mm}^{-1}$  grating is used to disperse the scattered light, which is then focused onto the CCD detector.

For the filter imaging mode (b), the laser spot size used to illuminate the sample is defocused to provide a diameter of 200  $\mu\text{m}$  using a 20 $\times$  objective lens. After passing through a holographic notch filter, which is the same as for the spectroscopic mode, the scattered Raman light is then transferred through a set of high-throughput tunable dielectric filters. These filters can be set to a given wavelength of a Raman band with a bandpass of 20  $\text{cm}^{-1}$ . At this point, the two-dimensional spatial information is maintained in the image while the third dimension, i.e., spectroscopic, is handled by the filters. The only light passing through the filters is radiation at the Raman band wavelength. The CCD detects, as for the spectroscopic mode, the two-dimensional image of the Raman light, with the x and y coordinates representing the spatial dimensions of the sample under the microscope.

The detector used is a Peltier-cooled slow scan 384 x 576 pixel CCD camera system, with the CCD chip maintained at -70  $^\circ\text{C}$ . Under these conditions, the dark current for the camera is less than 0.001 e $^-$ /pixel/s and a readout noise of less than 10 e $^-$ .

The dispersion of the detector is  $1.75 \text{ cm}^{-1}/\text{pixel}$  at the  $514.5 \text{ nm}$  wavelength for the spectroscopic mode. The collected light is digitized to 16 bits (65534 levels) before being returned to the computer via a 12 Mbaud serial link.

### **2.3. Subsystem 2. Electrochemical System**

The schematic model for the electrochemical glass cell was shown in Fig. 2.3.1. The  $\sim 7 \text{ mm}$  thick Pyrex glass cell has two arms, which are used for a reference electrode [saturated calomel (SCE) or  $\text{Ag}/\text{AgCl}$ ] and a counter electrode (platinum wire). The excitation laser light was focused on the sample through a quartz window, which has low fluorescence.  $20\times$  or  $50\times$  objective lenses are suitable for the electrochemical measurements. However, the  $100\times$  objective can only be used in air and not with a solution, because the working distance is too short for the electrochemical cell.

### **2.4. Subsystem 3. Point-by-Point Raman Imaging System**

The sample is placed underneath the objective lens on an XYZ stage (Newport, M-462-XYZ-M) equipped with stepper motors (Newport, 850B) which are controlled by a motion controller (Newport, PMC400). For obtaining a Raman spectrum, the sample is fixed relative to the stationary laser for the duration of the acquisition time. Next the sample is translated by a given distance and another Raman spectrum is acquired. This point-by-point Raman spectrum is used to build up a two-dimensional image. A Raman intensity image is generated by summing the data within a given spectral range. The main factor which determines the quality of a Raman image is the S/N ratio of each spectrum. Before performing the Raman imaging, a full Raman spectrum is initially

acquired to determine the location of the Raman peak(s). A spectral range corresponding to each Raman peak is determined and the data lying within each spectral band is collected and stored.

## 2.5. Subsystem 4. Photoelectrochemical Imaging System

Both the 351 and 364 nm lines of an Ar<sup>+</sup> laser (Coherent, Enterprise 622) at a power of 1 mW  $\mu\text{m}^{-2}$  are used in the photoelectrochemical measurements, i.e., photocurrent (or photovoltage) measurements. The laser lines used for both the Raman and photocurrent measurements are focused onto the sample using either the 20 $\times$  or the 50 $\times$  objective lens.

The photocurrent is measured using a lock-in amplifier (Stanford Research, SR850) and potentiostat (Hokuto Denko, HA150G). The incident light is modulated by means of a variable-speed mechanical chopper and controller (Stanford Research SR540). It should be noted that for photocurrent (or photovoltage) measurements, the resolution can also be controlled by the minority carrier diffusion length.

Both the Raman and the photocurrent images are taken over the same area of the sample in a glass electrochemical cell containing 0.05 M H<sub>2</sub>SO<sub>4</sub> aqueous solution. For the photocurrent measurements, an applied bias of 2 V (vs. SCE) is used.

The combination of the photoelectrochemical measurements and the Raman spectroscopy allows measurements over the same sample area, either simultaneously or sequentially. The procedures followed in the two measurements are slightly different. For semiconductors, the photoelectrochemical signals are usually large enough for measuring, and detection of these signals is much easier than that for the Raman signals and requires less collection time. In Fig. 2.5.1, the schematics of the two data collection procedures are shown. The photoelectrochemical data collection procedure consists of recording the signal while continuously moving the sample beneath a stationary laser and

their combining the scanned lines to form a two-dimensional image, as shown in Fig. 2.5.1a. For obtaining the Raman spectral data, the sample is fixed relative to the stationary laser for the duration of the acquisition time. Next, the sample is translated by a given distance and another Raman spectrum is acquired. These point-by-point Raman spectra are used to build up a 2-dimensional image, as shown in Fig. 2.5.1b. In a typical photoelectrochemical experiment, where a  $2\text{ mm} \times 2\text{ mm}$  area is scanned at a rate of  $50\text{ }\mu\text{m/s}$ , the time required is approximately 3.5 hours. The line scans are usually  $10\text{ }\mu\text{m}$  apart, and, for each line scan, 20,480 data points (40 seconds at a 512 Hz reading rate) are collected for each photocurrent (or photopotential) and phase angle. Thus, a data point is collected every  $0.1\text{ }\mu\text{m}$ , and roughly 100 data points are averaged to yield a  $10\text{ }\mu\text{m}$  resolution along each line scan. On the other hand, the point-by-point Raman spectral measurement requires roughly 23 hours for a  $2\text{ mm} \times 2\text{ mm}$  area, with a  $10\text{ }\mu\text{m}$  separation between data points (for a total of 40,000 data points) and a 1 s exposure time. For a 1 s exposure time, each data point requires a total time of approximately 2 seconds due to the time required for data storage, for moving to the next point, and for graphics operations that plot the most recently collected data on the monitor. For samples that are stable under illumination, the photoelectrochemical and Raman signals can be obtained simultaneously, where the sample is moved point-by-point under the stationary laser and is kept at that particular position for the duration of the exposure time.

## 2.6. Subsystem 5. Computer and Software

Subsystems 1-4 are controlled by a personal computer (IBM compatible, 486DX2 66MHz) using AT-GPIB interfaces. Either the personal computer or a workstation (Hewlett Packard, HP 9000 Series 700) are used for the curve-fitting program, in order to generate images of peak widths or the peak positions, with the advantages as described in Section 1.3 of Chapter 1.

The summation of intensities within a Raman peak is sufficient to yield the relative concentration of the species corresponding to the Raman band. However, if other pieces of information are desired, such as the widths of the peaks, or the locations of the peaks which can be related to the degree of crystallinity or stress, then it is necessary to curve-fit each spectrum to an analytical function, from which the peak widths and locations are obtained. For vibrational spectroscopy, the typical functions to use are the Gaussian and Lorentzian functions<sup>1-3</sup>, with the background described by a polynomial function. To obtain the best parameters, a nonlinear least-squares method has been used, i.e.,  $\chi^2$ , as defined below, is minimized :

$$\chi^2 = \sum_{i=1}^N \left[ \frac{y_i - Y_i[\mathbf{A}; x_i]}{w_i[\mathbf{A}; x_i; e_i]} \right]^2 \quad (2.6.1)$$

where N is the number of spectral data points in the spectrum,  $y_i$  is the intensity for spectral data point  $x_i$ ,  $Y_i[\mathbf{A}; x_i]$  is the calculated intensity for spectral data point  $x_i$ ,  $\mathbf{A}$  is the parameter vector (i.e., the peak width, intensity, and location),  $w_i$  is the weighting factor at spectral data point  $x_i$  which is the uncertainty in  $y_i$ , and  $e_i$  is the difference between  $y_i$  and  $Y_i[\mathbf{A}; x_i]$ . For an analytical function which consists of a Lorentzian function and a cubic polynomial  $Y_i[\mathbf{A}; x_i]$ , in equation (2.6.1) is given by:

$$Y_i[\mathbf{A}; x_i] = A_{3M+1} + A_{3M+2}x_i + A_{3M+3}x_i^2 + \sum_{j=1}^M \frac{A_{3j-2}A_{3j-1}^2}{[(x_i - A_{3j})^2 + A_{3j-1}^2]} \quad (2.6.2)$$

where M is the number of peaks, the  $A_{3j-2}$ 's are the peak widths, and the  $A_{3j}$ 's are the peak locations. Equation (2.6.1) has been minimized using the algorithm of Levenberg and Marquardt (or a gradient-expansion algorithm), which is a combination of a gradient-search procedure and a linearization of the analytical function, where-in the latter problem

of a nonlinear least-square fitting has been reduced to a linear least square fitting problem. This method has been shown to be fairly robust in most nonlinear least-squares fitting problems, provided that the initial parameter vector does not differ too greatly from the final parameter vector. To generate images of the various parameters, the full spectrum at each data point was taken, and then each spectrum was fitted to the analytical function given by equation (2.6.2).

### References

- 1 P. Gans and J. B. Gill, *Appl. Spectrosc.* **31**, 451 (1977).
- 2 W. F. Maddams, *Appl. Spectrosc.* **34**, 245 (1980).
- 3 L. Antonov and S. Stoyanov, *Appl. Spectrosc.* **47**, 1030 (1993).

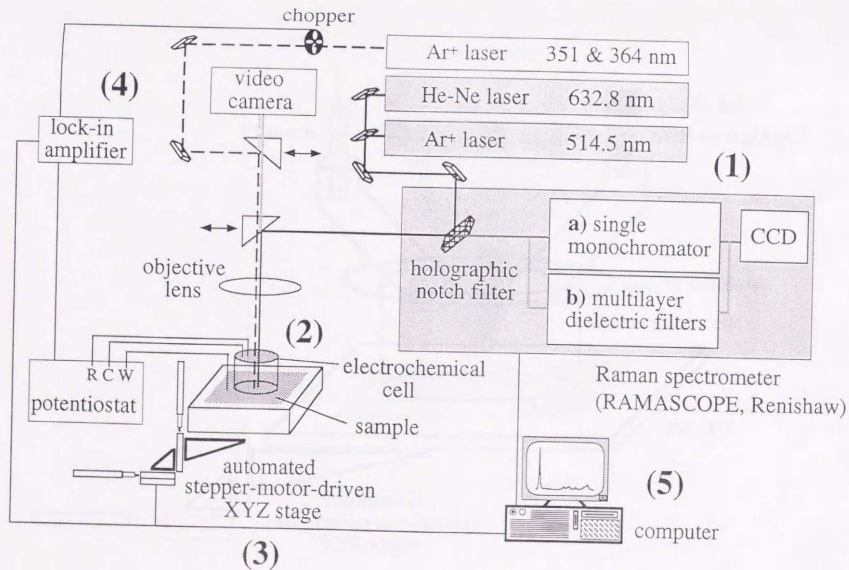


Figure 2.1.1. The experimental set-up of the new micro-Raman system, which is made up of five subsystems, i.e., (1) commercial Raman microscope with direct filter-imaging system, (2) electrochemical system, (3) automated point-by-point Raman mapping system, (4) photoelectrochemical imaging system, and (5) computer and software. Subsystems 1-4 are controlled by a computer using AT-GPIB interfaces.

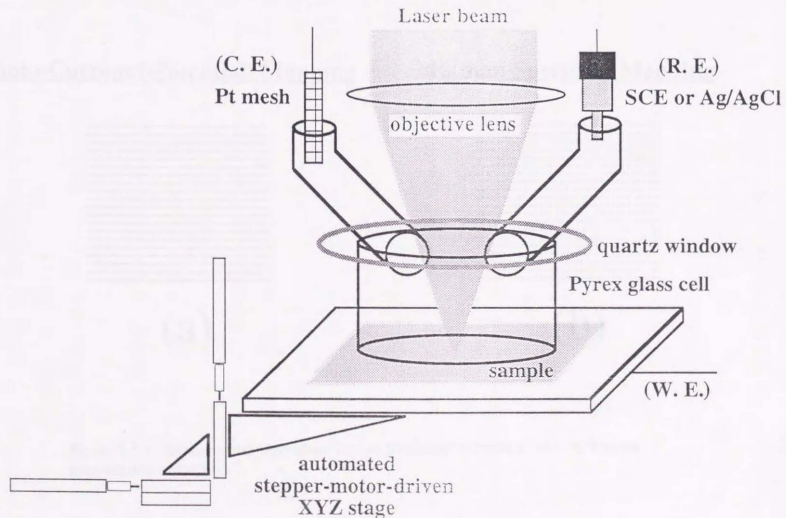
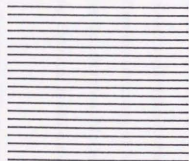


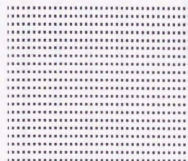
Figure 2.3.1 Glass electrochemical cell for micro-Raman spectroscopy. The cell is fixed on the automated stepper-motor-driven XYZ stage, which is used for the point-by-point mapping (see Section 1.3 of Chapter 1 and Section 2.4 of Chapter 2).

### Photo-Current (-Potential) Mapping



(a)

### Raman Spectrum Mapping



(b)

Figure 2.5.1 Experimental algorithms for (a) photoelectrochemical and (b) Raman mapping data collection.

## APPLICATIONS INVOLVING SURFACE PHENOMENA OF SEMICONDUCTORS USING NEW MICRO-RAMAN SYSTEM

### 3.1 Introduction

The author achieved the development of a the new Micro-Raman system and described many advantages for the study of surface phenomena of semiconductor and metal oxide materials in Section 1.3 of Chapter 1. In order to confirm the performance of the system, four significant examples obtained using this system are described in this chapter, including 1) photochromic properties of  $\text{MoO}_3$  films, 2) imaging analysis of microscale crystallization of  $\text{MoO}_3$  films, 3) combined Raman-photoelectrochemical imaging analysis of  $\text{TiO}_2$  films, and 4) strain imaging analysis of  $\text{Si}/\text{SiO}_2$  interfaces.

As described in Advantage 1 in Section 1.3, a high-sensitivity Raman system can lead to the use of relatively low power lasers which make it possible to measure colored materials without annealing and/or heating, e.g., photochromic or electrochromic colored amorphous materials, which are easily crystallized by high power lasers. In Section 3.2, Example 1, the author applied this Raman system to the study of amorphous  $\text{MoO}_3$  films in order to confirm the advantage of low power lasers. The results showed that the Raman spectra for the amorphous  $\text{MoO}_3$  films provided some new structural information on the reversible chemical modifications occurring during the coloration-bleaching process.

Another advantages of the system is the ability to do imaging, which is described in Advantage 2, Section 1.3. Raman imaging analysis is useful in providing structural information for semiconductor materials. The author observed the process of microscale

crystallization using the direct filter-imaging technique (included in Subsystem 1), as described in Section 3.3, Example 2.

Furthermore, the combined Raman-photoelectrochemical imaging system (including Subsystem 4) was developed in order to obtain the local spatial variation of the characteristics of heterogeneous semiconductor films. As a typical example, the comparison of the Raman images and photocurrent images of anodically formed  $\text{TiO}_2$  films is discussed in Section 3.4, Example 4.

Moreover, the author developed a strain-imaging system in order to detect high local stresses, which can give rise to defects in silicon substrates and can influence the electrical characteristics of devices. The results of two-dimensional Raman images of the variations in the Si Raman peak shift on an Al/SiO<sub>2</sub> patterned Si wafer are discussed in Section 3.5, Example 4.

The details of each of these examples are described in the next several sections.

### 3.2 Example 1.

#### A study of the photochromic properties of amorphous MoO<sub>3</sub> films using Raman microscopy

##### Introduction

Photochromism and electrochromism of transition metal oxides have received considerable attention because of potential applications in information display devices.<sup>1,2</sup> These oxides can be deeply colored with optical irradiation of the appropriate energy (photochromism) or with applied potential (electrochromism). WO<sub>3</sub><sup>3-9</sup> and MoO<sub>3</sub><sup>6,10-15</sup> have been the most extensively investigated materials of all the transition metal oxides. Deb<sup>16,17</sup> suggested that the color centers in WO<sub>3</sub> are due to electrons trapped at oxygen vacancies. Hurditch<sup>18</sup> demonstrated the dependence of coloration time and electrode potential on the water content of hydrated WO<sub>3</sub>·H<sub>2</sub>O films and postulated the reductive dissociation of H<sub>2</sub>O and formation of blue hydrogen tungsten bronze WO<sub>3-x</sub>(OH)<sub>x</sub> at the cathode. Faughnan et al.<sup>19</sup> proposed a model for the formation of the tungsten bronzes which involves the simultaneous injection of cations and electrons into the film. Similarly, in MoO<sub>3</sub> films, Zelaya-Angel et al. proposed molybdenum bronzes to be formed according to the reaction<sup>15</sup>:



(where A=H, Li, Na or Ag)

Fleisch and Mains<sup>6</sup> found that both crystalline MoO<sub>3</sub> and WO<sub>3</sub> powders turn blue upon UV irradiation in vacuum, and X-ray photoemission spectra supported the reversible formation of the +5 oxidation state, which was subsequently re-oxidized to the +6 oxidation state upon exposure to air. It is now accepted that, in photochemically colored MoO<sub>3</sub> (or WO<sub>3</sub>), the optical absorption is due to the intervalence charge transfer between Mo<sup>6+</sup> (or W<sup>6+</sup>) and the newly formed Mo<sup>5+</sup> (or W<sup>5+</sup>).<sup>19</sup> The photochromic properties

of amorphous MoO<sub>3</sub> (a-MoO<sub>3</sub>) films show faster response times for coloration than those of crystalline films<sup>3</sup> and thus the amorphous films are more suitable for use as memory devices. In addition, the UV-colored a-MoO<sub>3</sub> films show good stability in the air for long periods of time (up to several months).<sup>2</sup>

Despite extensive reported work on a-MoO<sub>3</sub> films in the literature, little has been reported on the structural properties of the colored films<sup>20,21</sup> and the structure of a-MoO<sub>3</sub> in the colored state still has not been clear. We have previously reported that photochemically colored films showed more ordering than those not exposed to UV irradiation, based on micro-Raman spectroscopic data.<sup>22</sup> This structural change of the colored films was, however, induced by laser annealing and was not directly related to the photochromic properties of the films, as will be shown in the present paper. In this paper we have used high-sensitivity Raman microscopy to investigate possible compositional or structural transformations of a-MoO<sub>3</sub> thin films accompanying the photochromic effects of UV irradiation.

## Experimental

The amorphous MoO<sub>3</sub> (a-MoO<sub>3</sub>) films were prepared by vacuum evaporation of high purity MoO<sub>3</sub> powder (99.9 %, Koso Chemicals Co., Ltd.) onto 1 mm thick ITO glass substrates (Asahi Glass Co., Ltd.), where the evaporation chamber was maintained at  $5 \times 10^{-5}$  Torr.<sup>2</sup> The thickness of the deposited films was about 1  $\mu$ m.

A 500 W high-pressure Hg lamp was used as the light source in the photochromic experiments. A band-pass filter centered at 350 nm with 100 nm FWHM (full width at half max.) was used to filter out visible and infrared light. The light power at the sample was measured with a power meter (MA10, Scientec) and found to be  $\sim 3$  mW/cm<sup>2</sup>. In order to observe the reversibility of the Raman spectra in the color-decolor cycles, the films were bleached electrochemically by applying a potential of +1.0 V vs. Ag/AgCl in 0.1 M LiClO<sub>4</sub>/propylene carbonate electrolyte. The counter electrode was Pt. After

bleaching the films, the electrolyte was removed from the glass cell in order to carry out subsequent photochromic experiments.

All absorbance measurements were performed on a UV-visible double-beam spectrophotometer (UV-3101PC, Shimadzu) using a sampling area of 12 x 2 mm. Since the absorbance and Raman measurements could not be conducted simultaneously due to the necessity of using exactly the same laser spot during a set of Raman measurements, as discussed later, the absorbance measurements were conducted independently of the Raman measurements using a separate sample cut from the same film but otherwise measured under the same conditions.

In this study, Subsystem 1 (except direct filter-imaging system), 2 and 5 shown in Fig. 2.1.1 of Chapter 2 were used for the Raman spectroscopic measurements. The Raman spectrometer used in this study was a Renishaw Ramascope. This spectrometer has high optical throughput and thus has the ability to obtain two-dimensional images.<sup>23-27</sup> The 514.5 nm line of an Ar<sup>+</sup> laser (Innova Enterprise Model 651, Coherent) at an output power of 100 mW was used as the excitation light source. The laser power was controlled from 0.05 mW to 45 mW using neutral-density filters. The light was focused onto the sample using a 100× objective lens mounted on an Olympus BH-2 optical microscope.

Each series of Raman measurements was carried out using a consistent spot position on the films for the photochromic as well as the crystallization processes in order to detect small changes in the Raman spectra. The size of the laser spot was ~2 μm with the 100× objective lens. To remove background signal, the spectrum of a clean ITO glass substrate was subtracted from all Raman spectra of the films. Cosmic ray lines, which are much sharper than Raman peaks, were removed from the data. Overlapped bands were resolved using a Lorentzian-curve fitting computer program provided by Renishaw.

## Results and Discussion

### A. Raman spectra of an amorphous MoO<sub>3</sub> film

A typical Raman spectrum for anhydrous crystalline MoO<sub>3</sub> powder is shown in Fig. 3.2.1a. Three sharp Raman peaks are clearly observed. These Raman bands are assigned to the terminal oxygen (Mo=O) stretching mode at 995 cm<sup>-1</sup>, the triply-connected bridge-oxygen (Mo<sub>3</sub>-O) stretching mode at 665 cm<sup>-1</sup>, and the doubly-connected bridge-oxygen (Mo<sub>2</sub>-O) stretching mode at 818 cm<sup>-1</sup>.<sup>28</sup> The sharpness of the peaks indicates that the corresponding vibrational modes are due to a highly ordered structure. Figure 3.2.1b shows a Raman spectrum of a vacuum-deposited amorphous MoO<sub>3</sub> film. An incident laser power of 0.05 mW was used to obtain this spectrum. There were no sharp Raman peaks, indicating an absence of a crystalline structure; however, three relatively broad peaks were found. Below the raw data, the deconvoluted peaks and the corresponding synthesized spectra are shown. We used three Lorentzian functions to fit the data. The synthesized spectra closely match the experimental data. The peaks at 700, 863, and 951 cm<sup>-1</sup> are analogous to those at 665, 818, and 995 cm<sup>-1</sup>, respectively, for crystalline MoO<sub>3</sub><sup>29,30</sup>, i. e., Mo<sub>3</sub>-O, Mo<sub>2</sub>-O and Mo=O, respectively.

The analysis of the known structural data on molybdic and tungstic compounds indicates common formation principles for these compounds. For example, both MoO<sub>3</sub> and WO<sub>3</sub> crystals are ReO<sub>3</sub>-related structures, having structures based on corner-sharing MO<sub>6</sub> octahedra. Moreover, MoO<sub>3</sub> possesses a unique layered structure of double chains of edge-sharing MoO<sub>6</sub> octahedra linked through vertices to form infinite corrugated layers held together by van der Waals forces.<sup>31</sup> Furthermore, the structures of the hydrated oxides such as MoO<sub>3</sub>·2H<sub>2</sub>O and MoO<sub>3</sub>·H<sub>2</sub>O are closely related to those of WO<sub>3</sub>·2H<sub>2</sub>O and WO<sub>3</sub>·H<sub>2</sub>O, respectively, and the amorphous films include these types of hydrated oxides.<sup>32</sup>

The structures of  $\alpha$ - $\text{MoO}_3$  and amorphous  $\text{WO}_3$  ( $\alpha$ - $\text{WO}_3$ ) have not been clearly determined, and many types of structural models have been proposed. Arnoldussen<sup>33</sup> suggested a molecular model consisting of trimeric  $\text{W}_3\text{O}_9$  molecules bound weakly to each other through water-bridge, hydrogen, and van der Waals bonding. Râmâns et al.<sup>32</sup> concluded from their micro-Raman study that the structure of  $\alpha$ - $\text{WO}_3$  films consists of a layer-type structure of tungsten hydrate and a framework-type structure of anhydrous tungsten trioxide. Similarly, the structure of vacuum-deposited  $\alpha$ - $\text{MoO}_3$  films is believed to consist of molybdenum hydrate and a framework structure of anhydrous molybdenum trioxide. Dickens et al.<sup>31</sup> reported that the water molecules in the structure of  $\text{MoO}_3 \cdot 2\text{H}_2\text{O}$  can be divided into two classes: (I) those between the layers and (II) those coordinated to the Mo atom, replacing the oxygen atom at the apex of the  $\text{MoO}_6$  octahedron. The terminal oxygen is located at the other apex of this octahedron and the layers are held together by hydrogen bonds. The structure of  $\text{MoO}_3 \cdot \text{H}_2\text{O}$  consists of layers of  $\text{MoO}_5(\text{OH}_2)$  corner-sharing octahedra.

In order to examine the film uniformity, spectra were obtained at several depths within a typical film, as shown in Figs. 3.2.2a-3.2.2c, in which spectra were deconvoluted from the raw spectra shown in Figs. 3.2.2a'-3.2.2c'. The focusing points were located on the surface and at 0.5 and 1  $\mu\text{m}$  below the surface of the film, respectively. Figs. 3.2.2b and 3.2.2c exhibit higher noise levels because of the reduced collection efficiency of the scattered light and reduced sampling volume in the irradiated area. All peak positions shown in Fig. 3.2 were obtained from the peak curve-fitting program. The differences between the three spectra in Figs. 3.2.2a-3.2.2c are negligible and indicate that the film was very uniform in the direction perpendicular to the film.

## **B. Properties of coloration-bleaching cycles and laser-induced crystallization of colored $\text{MoO}_3$ films**

The photochromic response of the film necessarily involves a change in the absorbance of the material. It was found that the colored films readily undergo

irreversible modifications upon laser irradiation due to absorption of the visible laser light. Before analyzing the Raman spectral changes due to the photochromic process, it is important to determine the proper level of incident laser power to be used for the Raman measurements in order to prevent annealing or crystallization. In this section we compare the crystallization process induced by laser annealing for the freshly-prepared vs. the colored films.

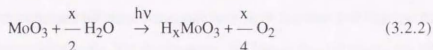
Figure 3.2.3 shows a series of the absorption spectra of the film during a coloration and bleaching cycle. Freshly-prepared  $\text{MoO}_3$  thin film is colorless, as shown in Fig. 3.2.3a. The sinusoidal modulation of the spectra is caused by interference effects. When the film is subjected to irradiation in air, the film turns blue. Figures 3.2.3b and 3.2.3c show the absorption spectra of the film after UV irradiation for 10 min. and 60 min., respectively. The longer irradiation time resulted in a larger photochromic response, as evidenced by the increase in the absorption. In the case of  $\text{MoO}_3$ , the maximum change occurs in the 800 - 850 nm range. The spectra for the films that were bleached electrochemically matched the original spectra before UV irradiation quite closely, demonstrating the reversibility of the cycle shown in Fig. 3.2.3d.

The annealing was induced by the same laser which was used in the Raman measurements, but at a much higher laser power. Figure 3.2.4 shows the Raman spectrum for a freshly deposited film (curve a), whose absorption spectrum corresponds to Fig. 3.2.3a, together with spectra obtained during the crystallization process. The incident laser power was sequentially increased from 0.05 mW to 45 mW, increasing the power after measuring each spectrum. Exposure times for annealing and Raman measurements were 20 min. each. All Raman spectra were measured with a laser power of 0.05 mW. From 0.05 mW to 10 mW, the film remained amorphous; however, starting at 25 mW, changes in the spectrum became evident. The amorphous peaks shifted slightly starting at 30 mW of incident laser power and sharper crystalline peaks became evident. At around 40 mW of irradiation, the film spectra became very similar to those for the crystalline material in Fig. 3.2.1a. Figure 3.2.5 shows a series of Raman

spectra for a colored film, whose absorption spectrum corresponds to Fig.3.2.3c., during the crystallization process. Even with as little as 5 mW of incident laser power, crystalline peaks became evident. With 10 mW of irradiation, the film spectra became similar to those of the crystalline material. These results indicate that the laser power should be less than 1 mW for a laser spot of  $\sim 1\mu\text{m}$  diameter ( $\sim 0.3\text{ mW}\mu\text{m}^{-2}$ ) in order to avoid modifying the film as a result of annealing during the Raman measurements.

### C. Structural dependence of photochromic properties

Oxidation states for Mo in hydrogen molybdenum bronze can include the +6, +5, and/or +4 when the  $\text{MoO}_3$  film is irradiated in air.<sup>14</sup> The adsorbed water on the  $\text{MoO}_3$  film is oxidized by the photogenerated holes when the semiconducting  $\text{MoO}_3$  is irradiated, releasing  $\text{O}_2$  and providing a source of protons and electrons.



The protons and electrons diffuse into the solid and form hydrogen bronze.

Figure 3.2.6 shows the change in absorbance measured at two wavelengths, [600 nm (open circles) and 800 nm (filled circles)] of an a- $\text{MoO}_3$  film as a function of irradiation time. A faster coloration response of coloration was found in the first 10 min., with coloration increasing more gradually with further irradiation. In addition, we reported that a measurement taken after 7 months of storage in the dark after the initial exposure revealed that the absorbance loss was less than 0.1 unit after coloration.<sup>15</sup> This result shows that the colored  $\text{MoO}_3$  film is stable in air and is capable of retaining its coloration memory for a long period of time. In addition to the color memory property, the  $\text{MoO}_3$  film also exhibits good reversibility in its coloration-decoloration process. After 60 min. of UV irradiation, the film can be electrolytically decolorized completely in a 0.1 M  $\text{LiClO}_4$ /propylene carbonate solution as shown, in Fig. 3.2.6. When the bleached film was subjected again to UV irradiation, the absorption spectrum of the colored film reverted back closely to its original form.

Figures 3.2.7a-3.2.7c show typical deconvoluted Raman spectra from raw spectra from 8a'-8c' for the MoO<sub>3</sub> film (a) before and after UV irradiation for (b) 10 min. and (c) 60 min. The spectra correspond to the points indicated by arrows a, b, and c in Fig. 3.2.6., respectively. The spectrum after electrolytic bleaching is shown in Fig. 3.2.7d. We found changes in both the Raman peak positions and the peak widths accompanying the coloration-bleaching cycles. The peak shifts are related to changes in the force constants of the bonds, i.e., positive and negative peak shifts correspond to larger and smaller force constants, respectively. The Raman band for the Mo<sub>2</sub>-O mode shifts toward lower wavenumber, from 863 cm<sup>-1</sup> in Fig. 3.2.7a to 853 cm<sup>-1</sup> in Fig. 3.2.7c during coloration and back to 863 cm<sup>-1</sup> in Fig. 3.2.7d after bleaching, which shows that the force constants for the Mo<sub>2</sub>-O bonds reversibly decrease and increase during the coloration-decoloration cycle. In addition, the Raman band shifts for the Mo<sub>3</sub>-O mode show that the force constants for these bonds also reversibly decrease and increase during the coloration-decoloration cycle. On the contrary, the Raman band shifts for the Mo=O mode show that the force constant for this bond reversibly increases and decreases during the cycle. A more detailed view of the relationship between the peak shifts and changes in absorbance is shown in Fig. 3.2.8. The shifts are proportional to the changes in absorbance, indicating that there was no phase transition. The standard deviations for several typical points were calculated from five separate data sets and are shown in Fig. 3.2.8, as indicated by error bars. This figure demonstrates that the peak shifts and thus the force constants for each bond are very sensitive to the state of coloration.

In order to establish the most probable location of protons which are injected into the a-MoO<sub>3</sub> film during UV irradiation, we next compare the Raman peak shift data for a-MoO<sub>3</sub> before and after coloration with calculated Mo-O bond strengths for crystalline MoO<sub>3</sub> and molybdenum hydrogen bronze. We also compare the present data with Raman results presented in the literature for these crystalline materials.

Dickens et al.<sup>31,34</sup> used neutron diffraction to determine crystal structures for two types of molybdenum bronzes, i. e., H<sub>0.36</sub>MoO<sub>3</sub>, and H<sub>1.68</sub>MoO<sub>3</sub>. The schematic model

of  $\text{H}_{0.36}\text{MoO}_3$ , low hydrogen content-type crystalline bronze is shown in Fig. 3.2.9. From the bond lengths, these authors used empirical bond-length to bond-strength correlations<sup>35</sup> to calculate the total bond strengths about each type of atom for  $\text{MoO}_3$ ,  $\text{H}_{0.36}\text{MoO}_3$  and  $\text{H}_{1.68}\text{MoO}_3$ , i.e., Mo, O(1) or triply coordinated, O(2) or doubly coordinated, and O(3) or singly coordinated. From the total bond strengths (t. b. s.) about the various types of oxygen atoms (shown as Table 3.2.1), they were able to infer the most probable positions for the hydrogen atoms. For lower hydrogen content, in the case of  $\text{H}_{0.36}\text{MoO}_3$ , the hydrogens appear to bond at O(2) or doubly coordinated, bridging oxygens ( see Fig. 3.2.9), judging from the low t. b. s. value (1.56) . For higher hydrogen content, however, as in the case of  $\text{H}_{1.68}\text{MoO}_3$ , the hydrogens appear to bond at O(3) or singly coordinated, bridging positions, judging from the low t. b. s. value of 0.41. Cotton and Wing<sup>36</sup> show that the bond orders for Mo-O bonds (i.e., strengths of individual bonds) are directly proportional to the vibrational force constants and can then in turn be related to the corresponding Raman shifts.

For the lower hydrogen content-type crystalline bronze, Eda<sup>37</sup> has confirmed that Raman shifts are consistent with bond strengths or bond orders predicted from the bond lengths (Table 3.2.1. The total bond strengths given in Table 3.2.1 for the various types of oxygens also show the trends.

The present results for the a- $\text{MoO}_3$  films also show trends which are consistent with those predicted and obtained for the crystalline materials (Table 3.2.1). During coloration, the  $\text{Mo}_2\text{-O}$  band [i.e., Mo-O(2)-Mo' stretch] shifts to lower wavenumber, which is consistent with the calculated t. b. s. and provides evidence for hydrogen being bonded to bridging oxygens in the amorphous film. During coloration the Mo=O band [i.e., Mo-O(3) stretch] shifts to higher wavenumber, which again is consistent with the calculated t. b. s., which shows a slight increase, from 2.05 to 2.12. It is also significant that the Mo=O band does not shift to much lower wavenumber, which would have been predicted if hydrogen were to have bonded at the terminal oxygen.

The t. b. s. values predict no change in the total bonding strength around the triply coordinated oxygens. The experimental result, however, showed a shift to lower wavenumber for the band assigned to the Mo<sub>3</sub>-O stretching mode. This may be related to the fact that the amorphous films are known to contain same hydrated MoO<sub>3</sub>,<sup>31</sup> in which there are no triply coordinated oxygens.

Figure 3.2.10 shows the changes in peak width for the (a) Mo=O, (b) Mo<sub>2</sub>-O, and (c) Mo<sub>3</sub>-O stretching modes during the photochromic process. All of the peaks became broader during the coloration process, which indicates that the number of defects in the structure increases during the coloration process. On the other hand, these peaks reversibly became sharper during the bleaching process. This result indicates that the more disordered structure in the colored state reversibly can revert back to the original structure. During coloration, some O(2) positions become bonded to hydrogen in the MoO<sub>3</sub> lattice, changing the bond lengths to those corresponding to the hydrogen bronze, thus leading to local distortions and wider Raman peaks.

The local bronze structures that are formed in the a-MoO<sub>3</sub> film are likely to be all of the same type as in the crystalline hydrogen molybdenum bronzes with lower hydrogen content, e. g., H<sub>0.36</sub>MoO<sub>3</sub>, because the number of these structures is low initially and the results indicate that these are no phase transitions, i.e., monotonically increasing peak shifts with increasing absorbance. Furthermore, the directions of the peak shifts during the coloration of the a-MoO<sub>3</sub> are consistent with those expected and experimentally found for the crystalline molybdenum bronzes with lower hydrogen content compared to the parent MoO<sub>3</sub>.

## Conclusions

The Raman spectra for the a-MoO<sub>3</sub> films provide some new structural information on the reversible chemical modifications occurring during the coloration-bleaching process. The Mo=O and Mo<sub>2</sub>-O peak shifts during the coloration process are consistent with the structure of the crystalline bronze, H<sub>0.36</sub>MoO<sub>3</sub>, in which the protons form -OH

bonds at bridging oxygen atoms. The Raman peaks for the amorphous  $\alpha$ - $\text{MoO}_3$  become broader during the coloration process and become reversibly sharper during the bleaching process. These results indicate that the number of defects or the local disorder in the framework structure of  $\text{MoO}_3$  increases during the photochromic process, but that the additional disorder again reversibly decreases upon bleaching.

## References

- 1 R. J. Colton, A. M. Guzman, and J. W. Rabalais, *Acc. Chem. Res.* **11**, 170 (1978).
- 2 J. N. Yao, K. Hashimoto, and A. Fujishima, *Nature* **355**, 624 (1992).
- 3 I. Shimizu, M. Sihizukuisi, and E. Inoue., *J. Appl. Phys.* **50**, 4027 (1979).
- 4 R. J. Colton, A. M. Guzman, and J. W. Rabalais, *J. Appl. Phys.* **49**, 409 (1978).
- 5 N. N. B. Dinh, V. T.; Hoang, N. H.; Minh, L. Q., *Phys. Stat. Sol. (a)* **108**, 157 (1988).
- 6 T. H. Fleisch and G. J. Mains, *J. Chem. Phys.* **76**, 780 (1982).
- 7 T. Oi, K. Miyauchi, and K. Uehara, *J. Appl. Phys.* **53**, 1823 (1982).
- 8 H. J. Stoker, S. Singh, L. G. Van-Uitertt, and G. J. Zydzik, *J. Appl. Phys.* **50**, 2993 (1979).
- 9 N. Yoshiike and S. Kondo, *J. Electrochem. Soc.* **130**, 2283 (1983).
- 10 T. C. Arnoldussen, *J. Electrochem. Soc.* **123**, 527 (1976).
- 11 N. M. Baba, S.; Nishiyama, N., *Jpn. J. Appl. Phys.* **23**, L638 (1984).
- 12 P. Pichat, M. Mozzanega, and C. Hoang-Van, *J. Phys. Chem.* **92**, 467 (1988).
- 13 J. W. Rabalais, R. J. Colton, and A. M. Guzman, *Chem. Phys. Lett.* **29**, 131 (1974).

- 14 J. N. Yao, B. H. Loo, and A. Fujishima, *Ber. Bunsenges. Phys. Chem.* **94**, 13 (1990).
- 15 O. Zelaya-Angel, C. Menezes, F. Sánchez-Sinencio, and G. F. L. Ferreira, *J. Appl. Phys.* **51**, 6022 (1980).
- 16 S. K. Deb, *J. Chem. Phys.* **37**, 4818 (1966).
- 17 S. K. Deb, *Phil. Mag.* **27**, 807 (1973).
- 18 R. Hurditch, *Electron. Lett.* **11**, 142 (1975).
- 19 B. W. Faughnan, R. S. Crandall, and P. M. Heyman, *RCA Rev.* **36**, 177 (1975).
- 20 P. Delichere, P. Falras, M. Froment, A. H. Goff, and B. Agius, *Thin Solid Films* **161**, 35 (1988).
- 21 M. F. Daniel, B. Desbat, J. C. Lassegues, and R. Garic, *J. Solid State Chem.* **73**, 127 (1988).
- 22 B. H. Loo, J. N. Yao, H. D. Coble, K. Hashimoto, and A. Fujishima, *Appl. Surf. Sci.* **81**, 175 (1994).
- 23 K. Ajito, J. P. H. Sukamto, L. A. Nagahara, K. Hashimoto, and A. Fujishima, *J. Electroanal. Chem.* **386**, 229 (1995).
- 24 K. Ajito, J. P. H. Sukamto, L. A. Nagahara, K. Hashimoto, and A. Fujishima, *J. Vac. Sci. Technol. A* **13**, 1234 (1995).
- 25 A. Fujishima, L. A. Nagahara, H. Yoshiki, K. Ajito, and K. Hashimoto, *Electrochim. Acta* **39**, 1229 (1994).
- 26 K. P. J. Williams, G. D. Pitt, B. J. E. Smith, A. Whitley, D. N. Batchelder, and I. P. Hayward, *J. Raman Spectrosc.* **25**, 131 (1994).
- 27 P. D. Wang, C. Cheng, C. M. S. Torres, and D. N. Batchelder, *J. Appl. Phys.* **74**, 5907 (1993).
- 28 I. R. G. Beattie, T. R., *J. Chem. Soc. (A)*, 2322 (1969).
- 29 H. Jezirowski and H. Knozinger, *J. Phys. Chem.* **83**, 1166 (1979).

- 30 J. M. Stencel, L. E. Makovsky, T. A. Sarkus, J. de Vries, R. Thomas, and J. Moulijin, *J. Catal.* **90**, 314 (1984).
- 31 P. G. C.-B. Dickens, S.; Weller, M. T., *Solid State Ionics* **18/19**, 89 (1986).
- 32 G. M. Ramāns, J. V. Gabrusenoks, and A. Vespāls, *Phys. Stat. Sol. (a)* **74**, 41 (1982).
- 33 T. C. Arnoldussen, *J. Electrochem. Soc.* **128**, 117 (1981).
- 34 P. G. Dickens, J. J. Birtill, and C. J. Wright, *J. Solid State Chem.* **28**, 1185 (1979).
- 35 I. D. Brown and R. D. Shannon, *Acta Cryst.* **A29**, 266 (1973).
- 36 F. A. W. Cotton, R. M., *Inorg. Chem.* **4**, 867 (1965).
- 37 K. Eda, *J. Solid State Chem.* **98**, 350 (1992).

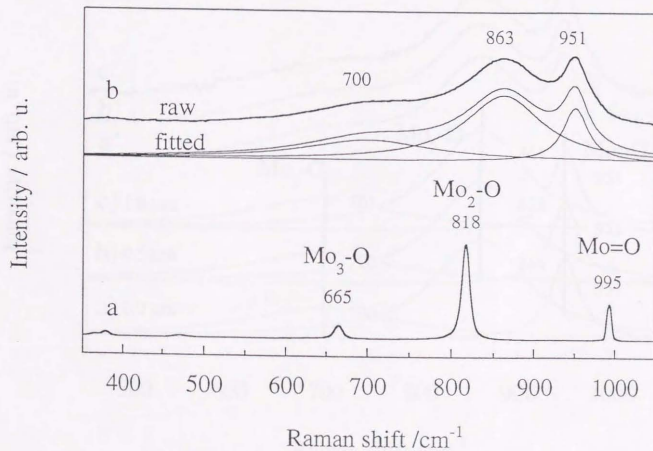


Figure 3.2.1. Raman spectra for (a)  $\text{MoO}_3$  crystalline powder and (b) vacuum-deposited  $\text{MoO}_3$  film. The deconvoluted component peaks plus the fitted spectrum are shown below the curve b.

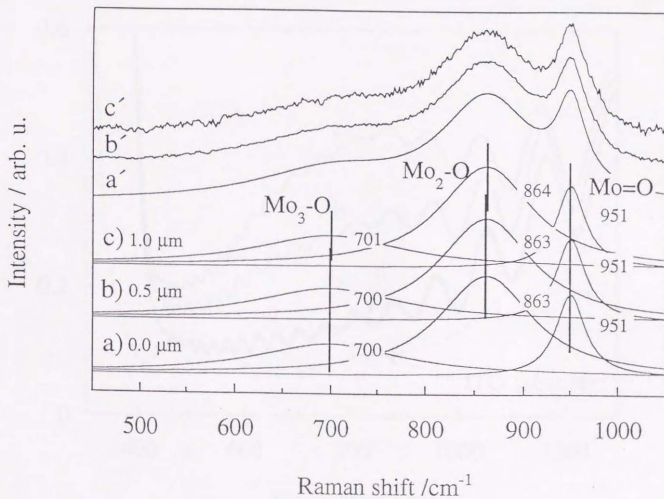


Figure 3.2.2. Raman spectra for an a-MoO<sub>3</sub> film which was sampled by adjusting the focal point (a) 0, (b) 500, and (c) 1000 nm below the surface. The deconvoluted components are shown in curves (a)-(c).

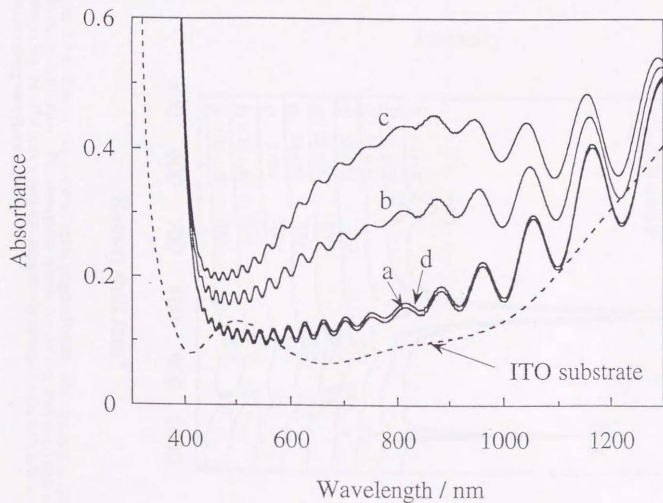


Figure 3.2.3. Absorption spectrum of a  $\text{MoO}_3$  film freshly prepared by vacuum evaporation on an ITO glass substrate (curve a). Curves b and c show the absorption spectra after UV irradiation for 10 min. and 60 min., respectively. Curve d shows an absorption spectrum obtained after complete electrolytical decoloration at an applied voltage of +1.0 V (vs. Ag/AgCl) for 5 min. in 0.1 M  $\text{LiClO}_4$ /propylene carbonate solution.

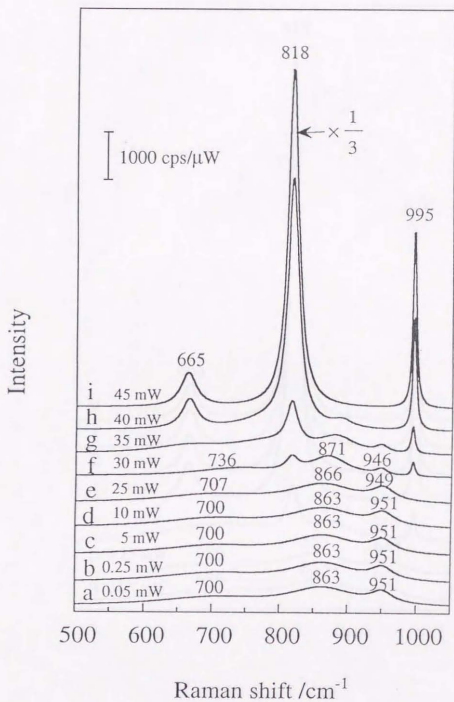


Figure 3.2.4. Raman spectra for a freshly prepared MoO<sub>3</sub> film obtained during laser-induced crystallization. The absorption spectra for the film before crystallization is shown in Fig. 3a. The laser power was sequentially increased from 0.05 mW to 45 mW after measuring each Raman spectra.

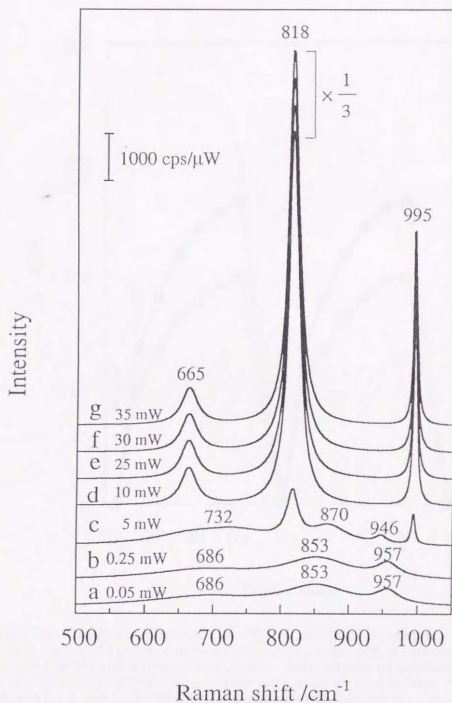


Figure 3.2.5. Raman spectra for a colored  $\text{MoO}_3$  film obtained during laser-induced crystallization. The absorption spectra of the film before crystallization was shown in Fig. 3.2.3c. The laser power used to induce crystallization was sequentially increased from 0.05 mW to 35 mW after measuring each of the Raman spectra, which were obtained at 0.05 mW laser power.

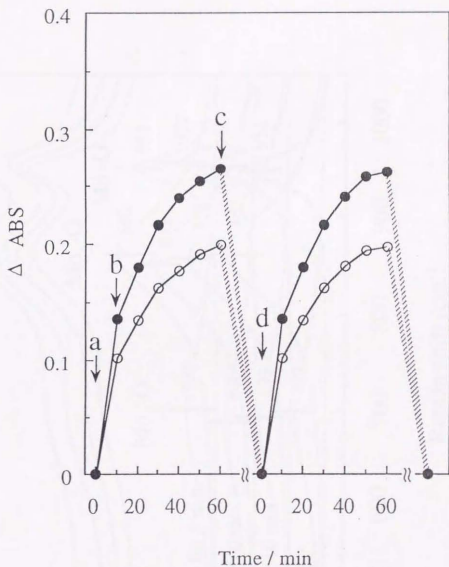


Figure 3.2.6. Changes in absorbance ( $\Delta \text{ABS}$ ) for an  $\alpha\text{-MoO}_3$  film during coloration and bleaching cycles, as a function of the irradiation time measured, at two wavelengths, 800 nm (filled circles) and 600 nm (open circles). After 60 min. of irradiation the colored film was electrolytically decolorized completely at an applied voltage of +1.0 V (vs.  $\text{Ag}/\text{AgCl}$ ) for 5 min. in 0.1 M  $\text{LiClO}_4$ /propylene carbonate solution (indicated by dash lines). Points a-d correspond to the full spectra shown in Fig. 3.2.3

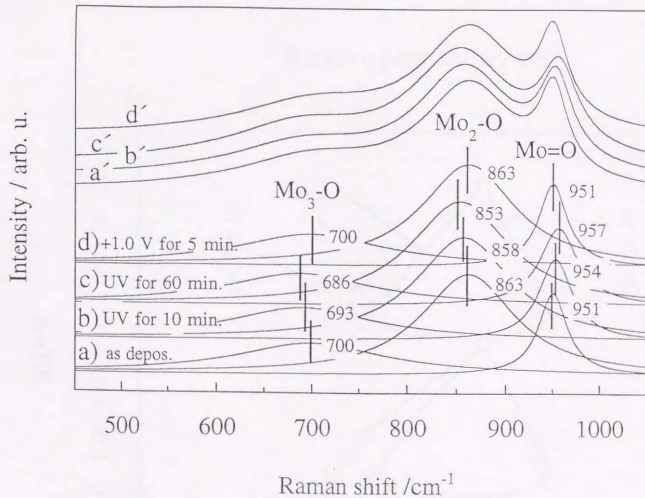


Figure 3.2.7. Deconvoluted Raman spectra for the  $\text{MoO}_3$  film (a) before and after UV irradiation for (b) 10 min. (c) 60 min., and (d) after electrochemical bleaching. These were calculated from the raw spectra shown in curves (a') - (d'), respectively. UV intensities and electrochemical conditions were the same as those in Fig. 3.2.6.

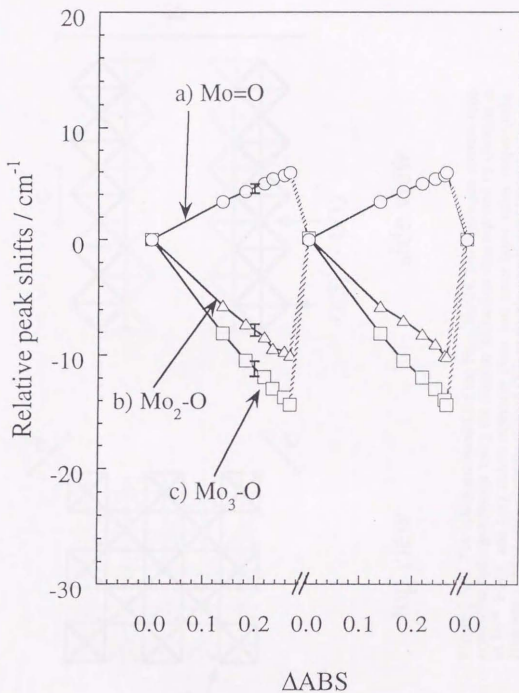


Figure 3.2.8. Relative peak shifts for the peaks corresponding to the (a) Mo=O, (b) Mo<sub>2</sub>-O, (c) Mo<sub>3</sub>-O stretching modes during the photochromic process. UV intensities and electrochemical conditions were the same as those in Fig. 3.2.6.

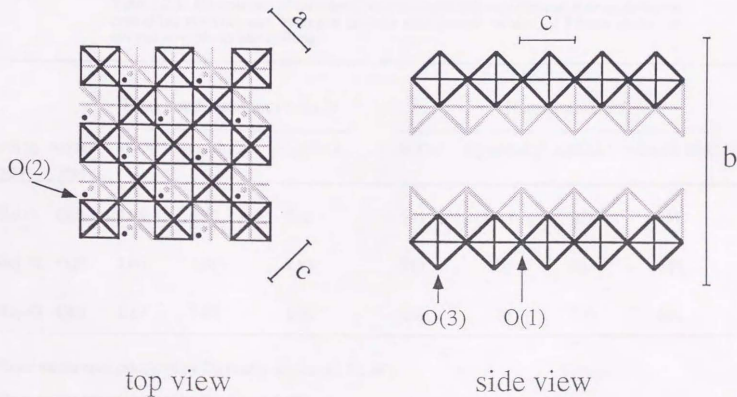


Figure 3.2.9. The schematic model for the  $H_{0.36}MoO_3$ , low hydrogen content-type crystalline hydrogen bronze using the neutron diffraction data reported by Dickens et al.<sup>31,34</sup> Black and gray colors represent outer and inner layer sides, respectively. Hydrogens (filled circles) appear to bond O(2) or doubly coordinated bridging oxygens. Some of hydrogen sites are occupied below 0.36 hydrogen content.

Table 3.2.1. Comparison of calculated bond strengths and experimental Raman shifts for crystalline molybdenum hydrogen bronzes with present results for Raman shifts for colored amorphous MoO<sub>3</sub> films.

bonding type	oxygen type	Total bond strength (t. b.s.) <sup>a</sup>			Raman shifts(cm <sup>-1</sup> )			
		MoO <sub>3</sub>	H <sub>0.36</sub> MoO <sub>3</sub>	H <sub>1.68</sub> MoO <sub>3</sub>	MoO <sub>3</sub> <sup>b</sup>	H <sub>0.30</sub> MoO <sub>3</sub> <sup>b</sup>	a-MoO <sub>3</sub> <sup>c</sup>	colored a-MoO <sub>3</sub> <sup>c,d</sup>
Mo=O	O(3)	2.05	2.12	0.41	995	1011	951	957
Mo <sub>2</sub> -O	O(2)	2.00	1.56	1.94	819	750	863	853
Mo <sub>3</sub> -O	O(1)	1.89	1.89	1.92	666	670	700	686

<sup>a</sup> These values were calculated by Dickens et al.(see ref. 31, 34).

<sup>b</sup> These values were measured by Eda (see ref. 37).

<sup>c</sup> Present work.

<sup>d</sup> UV irradiation time was 60 min. in the air.

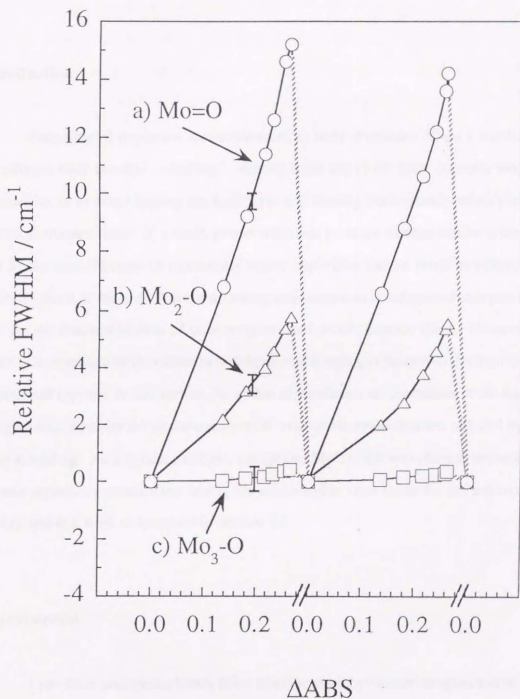


Figure 3.2.10. Changes in the FWHM (full width at half max.) for the peaks corresponding to the (a) Mo=O, (b) Mo<sub>2</sub>-O, (c) Mo<sub>3</sub>-O stretching modes during the photochromic process. UV intensities and electrochemical conditions were the same as those in Fig. 3.1.6.

### 3.3 Example 2.

#### Raman imaging analysis of microscale crystallization of MoO<sub>3</sub> thin films

##### Introduction

Annealing of implanted semiconductors by laser irradiation offers a number of advantages over thermal annealing.<sup>1</sup> Among these are 1) the laser intensity may be selected so as to avoid heating the base layer and thereby inadvertently modifying its electrical characteristics, 2) a much greater reduction in lattice damage can be achieved, and 3) the concentration of electrically active impurities can be made to exceed the solubility limit of the host. Raman scattering measurements is recognized as a powerful tool for the characterization of laser-recrystallized semiconductor films.<sup>2</sup> However to make this technique more viable, two-dimensional imaging is needed to distinguish the crystallized regions. In this section, the author demonstrates the usefulness of the Raman imaging technique for the characterization of microscale crystallization induced by the laser annealing. As a typical example, amorphous MoO<sub>3</sub> film was chosen, because the Raman signals of crystallized MoO<sub>3</sub> are much higher than those for the amorphous MoO<sub>3</sub>, and this work is described in Section 3.2.

##### Experimental

1  $\mu\text{m}$  thick amorphous MoO<sub>3</sub> films were prepared by vacuum evaporation of high purity MoO<sub>3</sub> powder (99.9 %, Koso chemicals Co., Ltd.) onto 1 mm thick ITO glass substrates, where the evaporation chamber was maintained at  $5 \times 10^{-5}$  Torr.<sup>3</sup> Since crystallization of freshly prepared MoO<sub>3</sub> films with laser annealing was found to be

difficult due to their transparency, the films were reduced electrochemically in a solution of 0.1 M LiClO<sub>4</sub> in propylene carbonate. As Mo<sup>6+</sup> was reduced to Mo<sup>5+</sup>, the film color changed to blue<sup>4,5</sup> and hence the optical absorption within the oxide increased. The films were reduced galvanostatically at -30  $\mu\text{A} / \text{cm}^2$  for 60 min.

In this study, Subsystems 1, 2, and 5, shown in Fig. 2.1.1, were used for the Raman spectroscopic and imaging measurements. The 514.5 nm line of an Ar<sup>+</sup> laser, at a power density of 1.6 mW  $\mu\text{m}^{-2}$ , was used both to crystallize and to measure the Raman spectra of the MoO<sub>3</sub> films. The laser was focused down to a spot with a diameter of 2  $\mu\text{m}$  using a 50 $\times$  objective lens in the microprobe Raman spectrometer. The amorphous MoO<sub>3</sub> thin films were annealed (crystallized) by rastering a laser at a high speed (2  $\mu\text{m} / \text{s}$ ).

To obtain Raman images, the 632.8 nm line of a HeNe laser at a power density of 9  $\mu\text{W} \mu\text{m}^{-2}$  was used. A 20 $\times$  microscope objective lens was used to focus the laser. Two other objective lenses (40 $\times$ , 4 $\times$ ), located outside the microscope, were used in conjunction with a pinhole having a diameter of 10  $\mu\text{m}$  to expand the spot size. Images were measured using a spot with a diameter of approximately 70  $\mu\text{m}$ . A multilayer dielectric filter centered at 818  $\text{cm}^{-1}$  (20  $\text{cm}^{-1}$  bandwidth) was used to isolate the desired Raman shift, corresponding to the highest intensity vibrational peak for the MoO<sub>3</sub> crystal, which has been assigned to the Mo-O-Mo stretching mode. Raman images were taken with an exposure time of 300 seconds and they have a spatial resolution of 1  $\mu\text{m}$ .

## Results and Discussion

As described in the previous section, amorphous MoO<sub>3</sub> films were reduced in order to facilitate the crystallization process. We found that laser annealing of films prior to the reduction process produced no visible Raman peaks characteristic of crystallized MoO<sub>3</sub> films. A typical Raman spectrum of a crystallized region is shown in Figure 3.3.1

(solid line). These Raman bands are assigned to the molybdenum-terminal oxygen stretching mode at  $995\text{ cm}^{-1}$  ( $a_g, b_{1g}$ ), the doubly-connected bridge (Mo–O–Mo) stretching mode at  $818\text{ cm}^{-1}$  ( $a_g, b_{1g}$ ), and the triply-connected bridge stretching modes at  $470\text{ cm}^{-1}$  ( $a_g, b_{1g}$ ) and  $665\text{ cm}^{-1}$  ( $b_{2g}, b_{3g}$ ), in agreement with Raman spectra for  $\text{MoO}_3$  crystalline powder.<sup>6</sup> However, it should be noted that the peak width at  $818\text{ cm}^{-1}$  for the crystallized  $\text{MoO}_3$  film was much larger than that found for  $\text{MoO}_3$  crystalline powder, which suggests that the former was more defective. A Raman spectrum of a colored  $\text{MoO}_3$  thin film annealed at half the laser power used previously,  $0.8\text{ mW }\mu\text{m}^{-2}$ , is shown in Figure 3.3.1 (dashed line). No sharp peaks are seen, even after an irradiation time of 10 min., which indicates that the film remained amorphous. We believe that the broad bands at  $860\text{ cm}^{-1}$  and  $970\text{ cm}^{-1}$  for the amorphous  $\text{MoO}_3$  film are analogous to the bands at  $818\text{ cm}^{-1}$  and  $995\text{ cm}^{-1}$  for crystalline  $\text{MoO}_3$  powder. Furthermore, the shoulder near the  $818\text{ cm}^{-1}$  band for the crystallized film (solid line in Fig. 3.3.1) is approximately at  $840\text{ cm}^{-1}$ , which suggests that the crystallized film still retained some amorphous character.

As described previously, bands of crystallized material were created on amorphous  $\text{MoO}_3$  films by rastering a laser beam. An optical micrograph of a laser-annealed amorphous  $\text{MoO}_3$  film is shown in Fig. 3.3.2a. The area shown is roughly  $85\text{ }\mu\text{m}$  by  $85\text{ }\mu\text{m}$ . The lines shown are separated by 16, 14, 14, and  $12\text{ }\mu\text{m}$ . It should be noted that the freshly prepared amorphous  $\text{MoO}_3$  films were very smooth. However, after being immersed in the propylene carbonate solution ( $0.1\text{ M LiClO}_4$ ), narrow ( $\sim 0.2\text{ }\mu\text{m}$ ) cracks appeared. In Fig. 3.3.2a, the width of the cracks is wider than  $0.2\text{ }\mu\text{m}$ , which we believe is due to additional stress generated during the annealing process. This optical micrograph shows that the five crystallized bands cannot be easily distinguished.

A Raman image of the same area was also taken, and the result is shown in Fig. 3.3.2b. The brightness in the image indicates the degree of crystallization, where an area of higher degree of crystallization is shown as being brighter. It should be noted that the crystallized bands can be seen more clearly in Fig. 3.3.2b than in Fig. 3.3.2a. The

Raman image shown in Fig. 3.3.2b was obtained by subtracting a background Raman image centered at  $738\text{ cm}^{-1}$  from a Raman image centered at  $818\text{ cm}^{-1}$  in order to remove broad-band luminescence due to impurities. Additionally, amorphous Raman bands, which have almost the same intensities at  $818$  and  $738\text{ cm}^{-1}$ , were also removed in this process. The background Raman image centered at  $738\text{ cm}^{-1}$  (not shown) was uniform, i.e., the cracks seen in Fig. 3.3.2a were not seen. Since the Raman signal was mainly generated in the bulk of the material, in contrast to the optical micrograph, which was due to the reflectivity at the surface, this result suggests that the cracks seen in Fig. 3.3.2a are confined mainly to the surface. The lines near the top and bottom of Fig. 3.3.2b are not seen clearly since the laser spot was more uniform near the center and less so near the edge of the region shown. The white dots shown between the crystallized  $\text{MoO}_3$  bands occur randomly, and hence, they can be assumed to be due to cosmic lines. Cosmic lines which appear in Raman spectra can be easily removed since they are much sharper than Raman signals, but, in images, cosmic lines can only be removed by comparing a few images of the same region. The crystallized bands are seen to be non-uniform lengthwise; there are regularly spaced thinner sections that can be seen. This is an artifact due to the holographic rejection filter used to isolate the laser line, and it occurs when a highly reflective specimen is being examined. This problem is being corrected presently by Renishaw. According to the Raman image, the crystallized bands have a thickness of approximately  $4\text{ }\mu\text{m}$  except near the edge of the laser spot. The width of these bands is larger than that of the laser beam ( $2\text{ }\mu\text{m}$ ) used to produce them. We believe that this is due either to thermal diffusion effects or multiple reflectivity within the oxide in case the laser used in the annealing process had a non-normal incident angle, or both.

## Summary

We have demonstrate the application of Raman imaging analysis in the study of the crystallization process in semiconductors. In particular, we have studied the crystallization of amorphous  $\text{MoO}_3$  films by laser annealing. Raman imaging analysis was particularly well suited for our work due to the large difference in Raman signal intensity for the amorphous and crystallized regions, which allowed the use of a short exposure time. It was also well suited for our work because of the high spatial resolution of  $1 \mu\text{m}$ . This method can be easily applied to other semiconductor materials such as silicon.

## References

- 1 H. Engstrom and J. B. Bates, *J. Appl. Phys.* **50**, 2921 (1979).
- 2 S. Nakashima, Y. Inoue, and A. Mitsuishi, *J. Appl. Phys.* **56**, 2989 (1984).
- 3 J. N. Yao, B. H. Loo, K. Hashimoto, and A. Fujishima, *Ber. Bunsenges. Phys. Chem.* **95**, 557 (1991).
- 4 J. W. Rabalais, R. J. Colton, and A. M. Guzman, *Chem. Phys. Lett.* **29**, 131 (1974).
- 5 T. C. Arnoldussen, *J. Electrochem. Soc.* **123**, 527 (1976).
- 6 I. R. G. Beattie, T. R., *J. Chem. Soc. (A)*, 2322 (1969).

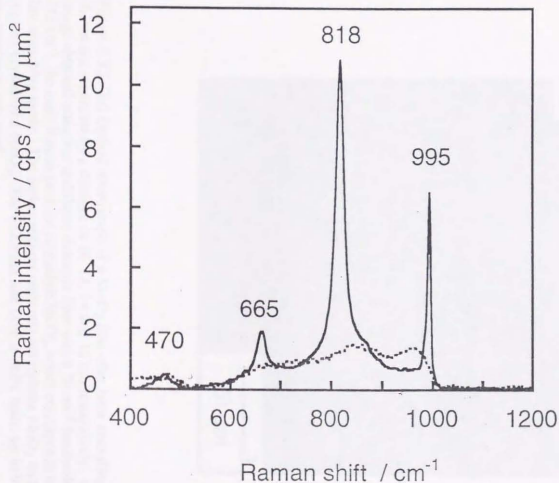


Figure 3.3.1. Raman spectra of a colored amorphous thin ( $\sim 1 \mu\text{m}$ ) film prepared by cathodic polarization at a constant current of  $30 \mu\text{A cm}^{-2}$  for 60 min. on vacuum evaporation before (dash line) and after laser annealing (solid line) with a spectral resolution of  $2 \text{ cm}^{-1}$ . The laser was focused to an area with a diameter of  $2 \mu\text{m}$  using a  $50\times$  objective lens. The laser power was set to give 0.8 and  $1.6 \text{ mW } \mu\text{m}^{-2}$  at the specimen. The  $514.5 \text{ nm}$  excitation from an  $\text{Ar}^+$  laser was used.

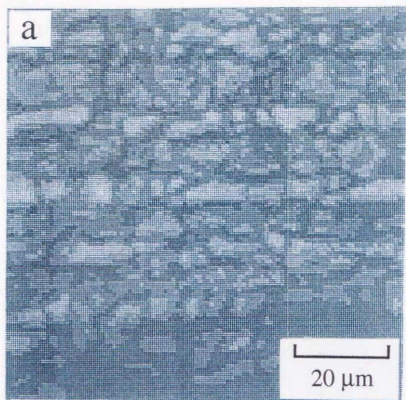
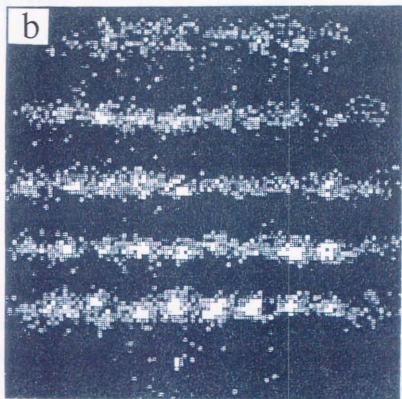


Figure 3.3.2. (a) Optical micrograph of a  $\text{MoO}_3$  film after laser annealing. The lines shown are separated by a distance of 16, 14, 14 and 12  $\mu\text{m}$  respectively. (b) A Raman image obtained using a multilayer dielectric filter with a  $20\text{ cm}^{-1}$  bandwidth centered at  $818\text{ cm}^{-1}$ , the main Raman peak for crystalline  $\text{MoO}_3$ , which corresponds to the Mo–O–Mo stretching mode. The darker regions represent amorphous  $\text{MoO}_3$  and the brighter regions crystallized  $\text{MoO}_3$ . The 632.8 nm line from a HeNe laser, set to  $9\text{ }\mu\text{W }\mu\text{m}^{-2}$  at the specimen, was used.



### 3.4 Example 3.

#### Combined Raman and photoelectrochemical imaging system.

#### Application to TiO<sub>2</sub> films grown anodically on Ti-Ag alloy

#### Introduction

TiO<sub>2</sub> is one of the most widely studied chemical substances due its favorable physical, optical and electronic properties. Numerous applications utilizing these properties include such areas as photocatalysis (e.g., photodegradation of organic compounds<sup>1-3</sup> and solar energy conversion<sup>4</sup>), corrosion-resistance in chemical reactor design,<sup>5</sup> and electronic devices.<sup>6</sup> In recent years an impressive array of analytical techniques has been utilized to investigate the properties of anodic films formed on titanium surfaces, such as Raman spectroscopy,<sup>7</sup> photoelectrochemical microscopy<sup>8</sup> and ellipsometry.<sup>9</sup> Of particular interests in fundamental studies are (1) the electronic properties (e.g., the densities of dopants and trap centers), (2) the optical properties (e.g., the refractive index), and (3) the structural properties (e.g., the phase and the composition) of these films.

A key factor in studying these oxide films is the ability to conduct the investigation *in-situ* and avoid the complications associated with ex-situ techniques such as possible changes in the film structure.<sup>10,11</sup> Two *in-situ* methods that have been commonly used in the study of oxide films are Raman spectroscopy and photocurrent (or photovoltage) measurements. Raman spectroscopy is useful in providing structural information of semiconductor materials such as the composition<sup>12</sup> and the phase.<sup>7</sup> On the other hand, photocurrent measurements are very useful in studying the electronic properties (e.g., the densities of dopants and trap centers) of dielectrics.<sup>13-15</sup>

Considerable improvement in these techniques over the past few years has made it possible to acquire *in-situ* two-dimensional images. Raman images<sup>16,17</sup> and photocurrent images<sup>18,19</sup> are useful for obtaining the local spatial variation of the characteristics of a heterogeneous semiconductor films.

In order to better understand the properties of these films, we developed a system combining Raman and photoelectrochemical imaging measurements. The advantage of this system is to compare directly the *in-situ* Raman and photocurrent mapped images over the same area. In this paper, we apply this system to investigate an anodically grown TiO<sub>2</sub> films on Ti-Ag alloy substrates and determine the relationship between structure and photocurrent generation.

## Experimental

In this study, Subsystem 1 (except direct filter-imaging system), 2, 3, 4, and 5 shown in Fig. 2.1.1 were used for the Raman and photocurrent measurements. The 632.8 nm line of a He-Ne laser (NEOARK, NEO-30MS) at a power of 1 mW  $\mu\text{m}^{-2}$  was used as the excitation light source. On the other hand, both the 351 and 364 nm lines of an Ar<sup>+</sup> laser (Coherent, Enterprise 622) at a power of 1 mW  $\mu\text{m}^{-2}$  were used in the photocurrent measurement. The laser lines used for both the Raman and photocurrent measurements were focused onto the sample using the same 50 $\times$  objective lens mounted on an Olympus BH-2 microscope.

The TiO<sub>2</sub> film was anodically grown on a Ag-Ti alloy substrate. The Ag (15 wt.%) was mixed uniformly with the Ti before forming the alloy, after which the substrate (50 mm  $\times$  50 mm) was mechanically polished to a mirror-finish. Prior to anodization, the substrate was etched in two different solutions: (1) 5 wt.% HF and (2) 5 wt.% HF and 10 wt.% H<sub>2</sub>O<sub>2</sub>. The oxide was grown potentiostatically at 115 V (vs. a

300 × 300 mm Al mesh counter electrode) for 30 minutes in 1 M H<sub>2</sub>SO<sub>4</sub> aqueous solution.

The measurements of both Raman and photocurrent images were taken over the same area in a glass electrochemical cell containing 0.05 M H<sub>2</sub>SO<sub>4</sub> aqueous solution. In the experiments, a saturated calomel reference electrode (SCE) and platinum wire were used as the reference and counter electrode, respectively. The point-by-point Raman spectrum of a 2 mm × 2 mm area was collected at the open circuit potential with a 10 μm separation between data points and a 1 second exposure time. For the photocurrent measurements, an applied bias of 2 V (vs. SCE) was used with the 351 nm and 364 nm lines from the Ar<sup>+</sup> laser modulated by a mechanical chopper at 40 Hz.

## Results and Discussion

We have studied the anodically grown TiO<sub>2</sub> film on Ag-Ti alloy substrate using the above mentioned combined 2-dimensional systems. A typical Raman spectrum of the anodic TiO<sub>2</sub> film in 0.05 M H<sub>2</sub>SO<sub>4</sub> aqueous solution is shown as curve (a) in Fig. 3.4.1. The spectrum is acquired using an exposure time of 20 s and the 632.8 nm line of the He-Ne laser. The Raman spectra of rutile and anatase TiO<sub>2</sub> powders (analytical grade) are shown as curves (b) and (c), respectively, in the same figure. The Raman signal passing through the electrolyte aqueous solution and glass window of the electrochemical cell is about 3 times weaker than that in air. The Raman spectrum of the anodic TiO<sub>2</sub> film shows clearly that there is a mixture of both anatase and rutile phases. Five Raman peaks at 144, 196, 396, 517 and 639 cm<sup>-1</sup> can be assigned to the anatase phase, and the three Raman peaks at 236, 446 and 610 cm<sup>-1</sup> correspond to the rutile phase.<sup>7,20</sup> No silver oxide peaks are observed. Background scattering, which is caused by Rayleigh scattering and stray light, is higher for the TiO<sub>2</sub> film than that of the powders. In order to

identify the Raman scattering from the background scattering, we subtracted the intensity at around  $320\text{ cm}^{-1}$  from each of Raman bands.

Figures 3.4.2a and 3.4.2b are Raman intensity images taken over the same  $2\text{ mm} \times 2\text{ mm}$  area at  $144\text{ cm}^{-1}$  and  $446\text{ cm}^{-1}$ , respectively. The former corresponds to the anatase phase and the later to the rutile phase. Since the Raman intensity of a particular phase is proportional to the concentration of that phase, the brighter area corresponds to higher concentration of that phase as indicated in the scale beneath the image. In Fig. 3.4.2a many black spots with a diameter of  $50 - 100\text{ }\mu\text{m}$  are found as indicated by the arrows. This heterogeneity is related to silver inclusions in the alloy which show up as black spots in the image due to the reduced thickness of the  $\text{TiO}_2$  over the silver regions. Similar domain sizes are also seen in an optical microscope before polishing. Figure 3.4.2a shows that the concentration of anatase is relatively uniform while Fig. 3.4.2b shows that the concentration of the rutile phase is more heterogeneous. However, the same black spots indicated by the arrows in Fig. 3.4.2a are in the same locations as in Fig. 3.4.2b, supporting the idea of Ag inclusions in the alloy.

Nevertheless, there are much more darker areas in Fig. 3.4.2b that are larger than those in Fig. 3.4.2a. The large darker domains in Fig. 3.4.2b are also presumably related to variation in the silver concentration in the Ti-Ag alloy substrate which is revealed during oxide growth. The rate of dissolution of Ti and the rate of combination with oxygen are crucial factors in forming anodically grown  $\text{TiO}_2$  films on Ti metal. In the silver rich regions, oxygen evolution occurs more efficiently during anodic oxidation and less Ti is converted to  $\text{TiO}_2$ . Moreover the rutile phase is formed at a higher anodic potential than the anatase phase.<sup>7</sup> Hence the observed results indicate that a higher potential is needed to oxidize Ti in the brighter region in Fig. 3.4.2b and is consistent with the idea of having smaller amounts of rutile phase in silver rich regions.

Figure 3.4.2c shows the anodic photocurrent of the same area. As indicated in the scale beneath the image, high photocurrent areas are represented as bright regions. Since the anodic  $\text{TiO}_2$  film is a n-type semiconductor, the anodic photocurrent measured is due

to the flow of holes from the bulk oxide to the oxide/electrolyte interface. Thus, the result shown in Fig. 3.4.2c implies that for photoelectrochemical processes where the rate is determined by the flow and the reaction rate of holes, there are only certain regions that are very efficient in this anodically formed TiO<sub>2</sub> film. It can be seen that there are regions with extremely high photocurrents. The brighter spots indicated by the arrows in Fig. 3.4.2c correspond to the same black spots in Fig. 3.4.2a and 3.4.2b.

In photocatalytic reactions, it is well known that silver deposited TiO<sub>2</sub> powders shows higher efficiency in the decomposition of organic compounds than without any metal deposit.<sup>3</sup> It should be stressed here that the heterogeneity observed in the photocurrent image in Fig. 3.4.2c is correlated with the rutile concentration more than with the anatase concentration. However, this does not mean that charge separation and transportation processes are enhanced by the rutile phase, but rather accelerated by the silver under the TiO<sub>2</sub> surface. In general, photocatalytic reactions and photocurrent generation efficiency is lower with rutile than anatase.<sup>21</sup> This difference is usually ascribed to the difference of the band-structure and the adsorption property of reactants on the TiO<sub>2</sub> surface.<sup>1-3,21</sup> The photocurrent depends not only on the crystal phase or silver concentration, other factors, such as the doping density and the flat band potential, probably also contribute to the efficiency of photocurrent-generation and those dependences can be revealed through a more quantitative analysis of the Raman peaks. Such detailed experiments and analyses are under investigation.

## Summary

A two-dimensional imaging system combining photoelectrochemical and Raman spectroscopy techniques was constructed and used to investigate an anodically grown TiO<sub>2</sub> film on a Ti-Ag alloy substrate. *In-situ* measurements of both Raman and photocurrent images were acquired over the same 2 mm × 2 mm area in a 0.05 M H<sub>2</sub>SO<sub>4</sub>

aqueous solution. Heterogeneity of the film is found in both images and the comparison of the images indicates that the photocurrent is correlated more strongly with the rutile phase of  $\text{TiO}_2$  rather than the anatase phase. Areas with a higher photocurrent generation contain less rutile phase.

## References

- 1 *Photochemical Conversion and Storage of Solar Energy; Vol. 1*, edited by E. Pelizzetti and M. Schiavello (Kluwer, Dordrecht, 1991).
- 2 M. A. Fox and M. T. Dulay, *Chem. Rev.*, **341** (1993).
- 3 A. Wold, *Chem. Mater.* **5**, 280 (1993).
- 4 A. Fujishima and K. Honda, *Nature* **37**, 238 (1972).
- 5 R. D. Armstrong, J. A. Harrison, H. R. Thirsk, and R. Whitfield, *J. Electrochem. Soc.* **117**, 1003 (1970).
- 6 F. Huber, *J. Electrochem. Soc.* **115**, 203 (1968).
- 7 L. D. Arsov, C. Kormann, and W. Plieth, *J. Electrochem. Soc.* **138**, 2964 (1991).
- 8 M. R. Kozlowski, P. S. Tyler, W. H. Smyrl, and R. T. Atanasoski, *Surface Sci.* **194**, 505 (1988).
- 9 J. L. Ord, D. J. D. Smet, and D. J. Beckstead, *J. Electrochem. Soc.* **136**, 2178 (1989).
- 10 J. Gui and T. M. Devine, *J. Electrochem. Soc.* **138**, 1376 (1991).
- 11 A. Felske and W. J. Plieth, *Electrochim. Acta* **34**, 75 (1989).
- 12 D. Ham, Y. Son, and K. K. Mishra, *J. Electroanal. Chem.* **310**, 417 (1991).
- 13 *Semiconductor Electrochemistry, Comprehensive Chemical Kinetics; Vol. 27*, edited by A. Hamnett (Elsevier, Amsterdam, 1987).
- 14 W. J. Plieth, *Bull. of Electrochem.* **6**, 109 (1990).

- 15 F. D. Quarto, S. Piazza, and C. Sunseri, *Electrochim. Acta* **38**, 29 (1993).
- 16 K. Ajito, J. P. H. Sukanto, L. A. Nagahara, K. Hashimoto, and A. Fujishima, *J. Vac. Sci. Technol. A* **13**, 1234 (1995).
- 17 A. Fujishima, L. A. Nagahara, H. Yoshiki, K. Ajito, and K. Hashimoto, *Electrochim. Acta* **39**, 1229 (1994).
- 18 P. Schmuki and H. Böhm, *J. Electrochem. Soc.* **141**, 362 (1994).
- 19 D. E. Williams, A. R. J. Kucernak, and R. Peat, *Electrochim. Acta* **38**, 57 (1993).
- 20 L. D. Arsov, C. Kormann, and W. Plieth, *J. Raman Spectrosc.* **22**, 573 (1991).
- 21 J. Augustynski, *Electrochim. Acta* **38**, 43 (1993).

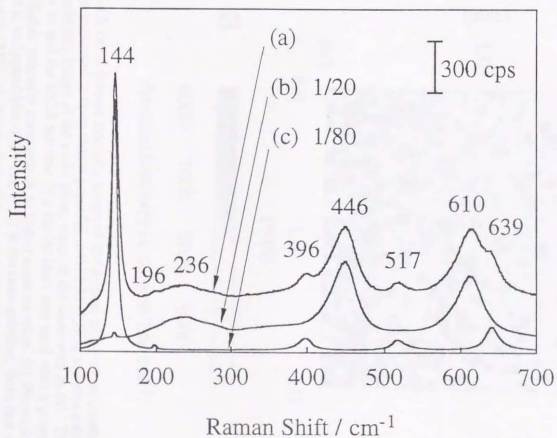


Figure 3.4.1. Typical Raman spectra of (a) an anodically grown  $\text{TiO}_2$  film on a Ti-Ag alloy substrate, (b) rutile powder, and (c) anatase powder. The exposure time was 20 seconds, and the 632.8 nm line of a He-Ne laser was used with a power of  $1 \text{ mW } \mu\text{m}^{-2}$ .

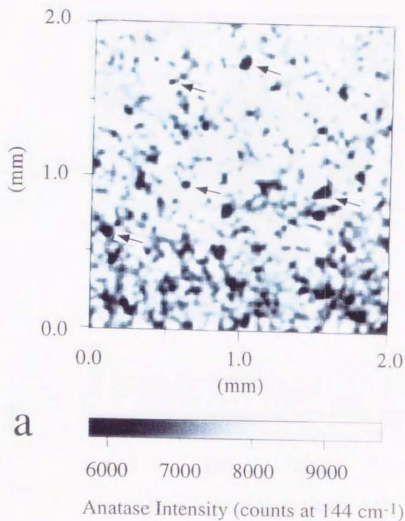
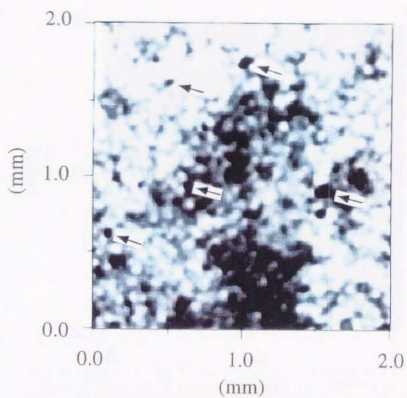
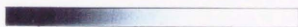


Figure 3.4.2. (a) A Raman intensity image of the anatase phase of an anodically grown  $\text{TiO}_2$  film measured at open circuit potential in 0.05 M  $\text{H}_2\text{SO}_4$  aqueous solution. (b) A Raman intensity image of the rutile phase taken in the same area as (a). The exposure time was 1 s and the 632.8 nm line of a He-Ne laser was used with a power of  $1 \text{ mW } \mu\text{m}^{-2}$ . Higher intensity corresponds to higher concentration. (c) Photocurrent image measured at an applied bias of 2V (vs. SCE) in the same solution. Scan rate was  $50 \mu\text{m} / \text{s}$ , and both the 351 and 364 nm lines of an  $\text{Ar}^+$  ion laser were used with a total power of  $1 \text{ mW } \mu\text{m}^{-2}$ . Brighter regions correspond to higher photocurrent areas.

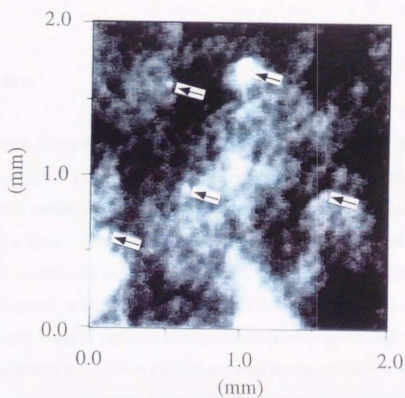


b

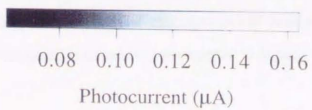


600 800 1000

Rutile Intensity (counts at  $446\text{ cm}^{-1}$ )



C



### 3.5 Example 4.

#### Strain imaging analysis of Si using Raman microscopy

##### Introduction

Although much attention has focused on the research and development of fabricating higher density and lower power semiconductor devices, there is also considerable interest in further improving the yield and durability of such devices. Failure in a device can occur at any number of stages before, during, and after fabrication. For instance, defects in the starting semiconductor material, misalignment of a photolithography mask, or improper metallization and passivation can all contribute to device failure. Another aspect of device failure is stress-related. High local stress can give rise to defects in the silicon substrate and even to structural defects such as breaking of the pad oxide,<sup>1</sup> which makes further processing impossible. Furthermore, mechanical stress is known to influence the electrical characteristics of devices. Metal-oxide-semiconductor (MOS) integrated circuits have been reported to degrade under mechanical stress.<sup>2,3</sup>

Raman spectroscopy is a useful and non-destructive diagnostic technique which can detect various types of defects resulting in device failure. De Wolf *et al.* have reported using micro-Raman spectroscopy to study mechanical stress in structures fabricated on silicon substrates.<sup>4,5</sup> However to make this technique more viable, two-dimensional mapping is needed to locate defective regions. In this section, we report on the acquisition and analysis of two-dimensional Raman imaging of an Al/SiO<sub>2</sub> patterned Si wafer. Two-dimensional images of the variations in the Si Raman peak intensity, shift, and broadening, which are related to changes in composition, stress, and crystallinity in the Si, respectively, are generated. Moreover, since the generation of

these images originates from the same spatial location, relationships between the various properties of Si and certain structural features can be drawn.

## Experimental

### A. Instrumentation and Sample

The AFM measurements were taken with a Seiko Instruments SPA 300 system under ambient conditions using commercially available  $\text{Si}_3\text{N}_4$  cantilevers. Images were obtained in a deflection mode with a small amount of integral gain. In this mode, the topography is determined by monitoring the difference in the light intensity reflected from the cantilever as it moves over the surface using a split photodiode. The small amount of gain created the effect of side-lighting the surface and enhanced contrast in the image.

In this study, Subsystem 1 (except direct filter-imaging system), 3 and 5 shown in Fig. 2.1.1 were used for the Raman and photocurrent measurements. The test sample used for Raman imaging is an Al patterned test pad on a Si (001) wafer. The substrate consists of a 500 nm thick thermal oxide layer grown on a Si (001) wafer on top of which a 400 nm thick Al layer was vacuum deposited at room temperature. No special cleaning treatment is used on the test sample prior to Raman imaging.

### B. Raman Image Acquisition

Figure 3.5.1 shows a typical Raman spectrum of a Si (001) single crystal. The peak height of the first order Raman peak of Si is about 1450 counts/s at  $520\text{ cm}^{-1}$  and the HWHM (half width at half maximum) is approx.  $2.4\text{ cm}^{-1}$ . Since the focal length of our monochromator is relatively short, the Raman band width of Si is broader than typically reported in the literature. The Raman peak position is calibrated using a standard neon emission source. Using our Raman system, 25 ms is sufficient to detect

the Raman signal of Si; however in order to calculate strain with a certain accuracy, a 250 ms exposure time is used to obtain a Raman spectrum at each point. Total exposure time to obtain the Raman data in a  $500\ \mu\text{m} \times 500\ \mu\text{m}$  area constructed from 10000 points is 2500 s. Each Raman spectrum is then fitted to a Lorentzian function and a background baseline to determine variations in three components of the Raman spectrum (i.e., intensity, width, and position).<sup>6-9</sup> These variations are related to the composition, defect density and the degree of stress. In the case of stress imaging, a relation exists between the stress,  $\tau$  (in Pa), and the Raman shift,  $\Delta\omega$  (in  $\text{cm}^{-1}$ ), of the signal. This relationship can be expressed by the following equation.<sup>10</sup>

$$|\tau| = 2.49 \times 10^8 \cdot \Delta\omega \quad (3.5.1)$$

A positive or negative shift in the Raman peak position corresponds to compressive and tensile stress, respectively.

## Results

### A. Raman intensity image of Si

Figure 3.5.2a shows an optical micrograph of the Al test circuit on a Si (001) wafer. The area shown is  $500\ \mu\text{m} \times 500\ \mu\text{m}$ . The darker regions correspond to areas of the bare Si substrate and the brighter regions correspond to areas of Al. The spatial resolution of the image is  $\sim 1\ \mu\text{m}$ . Figure 3.5.2b shows a raw data Raman intensity image of Si taken in the same area as Fig. 3.5.2a. Fluorescence signal caused by residual masking material or dust particles is removed by subtracting the background signal. The brighter regions in this image correspond to the strong Raman signal of the Si wafer. In the Al regions, no Raman signal is detected in same spectrum range as in

Fig. 3.5.1. This result shows that the thickness of the deposited Al film is sufficient to reflect completely the exciting laser light.

### B. Disorder image of Si

Variations in the HWHM of a Raman peak provide a degree of surface disorder induced during processing. The line width increases when a material is damaged or disordered, because these conditions increase phonon damping or change the rules for momentum conservation in the Raman process.<sup>11</sup> Figure 3.5.3a shows an image of the variation in the HWHM of the Si Raman peak in the same area as Fig. 3.5.2a. The black regions in Fig. 3.5.3a, corresponding to the brighter Al regions in Fig. 3.5.2a, have no data of the HWHM since the Raman signals cannot be obtained in these regions as mentioned above. Most of the sample looks very uniform, but several bright spots are seen which correspond to a wider HWHM. In this particular case, scratch marks in the Si wafer are the source of disorder in the film and are clearly evident from the image. A cross sectional profile, indicated by the black dash line in Fig. 3.5.3a, is shown in Fig. 3.5.3b. A very sharp peak is found in Fig. 3.5.3b at point X and corresponds to the damaged region in Fig. 3.5.2a. The width of the Raman line increases at point X which is due either to spatial inhomogeneity there (i.e., the presence of microcrystallite of various size) or the mixing of different types of stress. In the case of mixed stress, the peak shifts toward lower frequencies, from 515 to 519  $\text{cm}^{-1}$ , is also reported.<sup>12,13</sup>

### C. Strain image of Si

Figure 3.5.4a shows a Raman strain image of the sample as indicated by the relative Raman shift of Si. The area of this image is the same as that of the micrograph in Fig. 3.5.2a. The Raman shift of the Si substrate far from the Al circuits is set to 0.00  $\text{cm}^{-1}$ . The black regions in Fig. 3.5.4a, corresponding to the brighter Al regions in Fig. 3.5.2a, have no data of the Raman shift. Brighter areas represent the areas with positive peak shifts and corresponds to compressive stress. On the other hand, darker areas

represent negative peak shifts and corresponds to tensile stress. On the left edges of the Al circuit, some parts clearly show compressive stress. The cross sectional profile of the same region as Fig. 3.5.3b is shown in Fig. 3.5.4b. A positive  $1.04 \text{ cm}^{-1}$  peak shifts at point B occurring at the left side edge of the Al circuit is clearly observed. This peak shifts at point B corresponds to a compressive stress of  $2.59 \times 10^8 \text{ Pa}$  as calculated by eq. (1). A small negative peak shifts,  $-0.10 \text{ cm}^{-1}$ , is also seen (point A) besides point B. Similar pairs of peaks are also observed on the wafer as indicated by points E and F.

Around point G in Fig. 3.5.4b, slight compressive and tensile stress are found. This region corresponds to the very narrow Al pattern, as clearly seen in Fig. 3.5.2a. However, the same structure is difficult to see in Raman intensity image (Fig. 3.5.2c) due to the spatial resolution of the Raman system used in these experiments. Nonetheless, the outline of the Al pattern is observed in the stress image and presumably results from the stress distribution being wider than the area of Al pattern. The tensile stress at point D is related to the damaged region that has high degree of the surface disorder induced during processing shown at point X in Fig. 3.5.3b.

## Discussion

### A. Stress at the interface between the Si substrate and deposition layers

The coefficients of thermal expansion of Si and  $\text{SiO}_2$  are  $4.2 \times 10^{-6}$  and  $5.5 \times 10^{-5} \text{ K}^{-1}$ , respectively. The coefficients of thermal expansion of  $\text{SiO}_2$  is ten times larger than that of Si. Since the  $\text{SiO}_2$  layer is made by thermal oxidation, compressive stress of Si at room temperature will occur at the interface between the Si substrate and  $\text{SiO}_2$  film grown. In this particular sample, it is difficult to see the strain since the  $\text{SiO}_2$  film is covered by the Al which reflects the exciting laser light for the Raman measurement. However, strain is clearly observed along certain edges along the left side of the Al

circuit pattern. However the right, upper, and lower side of the Al pattern, hardly any stress is found.

Discrepancy between the left and right side of the Al pattern is difficult to discern in the optical micrograph (Fig. 3.5.2a) and thus the error in masking is less than 1  $\mu\text{m}$ . In order to study the origin of stress seen in Fig. 3.5.4a, atomic force microscopy (AFM) images were obtained along the edges of the Al pattern. Figure 3.5.5a shows an AFM images of the boundary region between deposited Al region and Si substrate. In this image, points A and B correspond to the same location as points A and B in Fig. 3.5.4b. Two deposition layers are found on Si substrate as clearly shown in Fig. 3.5.5a. The two layers result from the  $\text{SiO}_2$  layer (middle layer) not being completely covered by Al layer (top layer), indicating some error in alignment of the photolithography mask. On the contrary near point C, corresponding to that in Fig. 3.5.4b, the  $\text{SiO}_2$  layer is not observed (Fig. 3.5.5b). Figures 3.5.5a and 3.5.5b indicate that the Al layer was a misaligned toward the right by approximately 500 nm. A schematic model for this results is shown in Fig. 3.5.6. The compressive stress at Point B was detected because of the slight error in masking for the Al. On the contrary the compressive stress left of point C was hidden by Al. The small tensile stress at point A and point C were caused by the reaction of the compressive stress.

#### **B. Accuracy in the determination of the Raman peak position**

In order to discuss the Raman peak position calculated by a fitting program, it is important to verify the error associated with the fitted parameters. To determine this error, there are two possible procedures that can be followed: (a) repeat the measurement a number of times or (b) use Monte Carlo method.<sup>9,14-17</sup> The latter was chosen since it required less time for Raman measuring and Si is not stable under prolonged exposure using a strong laser. The Monte Carlo method used consists of generating a new set of data by randomly displacing the original spectrum at each spectral data point according to Poisson statistics (which is applicable to photon counting processes). That is,

$$y_i^{\text{new}} = y_i + s_j \quad \text{for } i = 1, \dots, N \quad (3.4.2)$$

where  $s_j$  is determined randomly according to Poisson statistics with a mean given by  $y_i$ . Results of a typical point cycled in 100,000 times showed that the error in determining the peak position is about  $0.07 \text{ cm}^{-1}$  standard deviation. So the stability of our system is about  $1.74 \times 10^7 \text{ Pa}$  as calculated using eq. (3.4.1).

### Conclusions

We have generated strain images of Al patterned test circuit on Si wafer using a modified micro-Raman microscope by combining a commercially-available high optical throughput spectrometer with Peltier cooled CCD detector and a XYZ stepper stage. Roughly a  $1 \text{ cm}^{-1}$  positive shifts, corresponding to  $2.49 \times 10^8 \text{ Pa}$  compressive stress, was clearly observed near the boundary of Al/SiO<sub>2</sub> film and bare Si wafer. Improper alignment of the masked used for the Al deposition was attributed to the features observed in the stress image. Continued improvements in Raman instrumentation should make this technique a valuable tool for failure analysis of devices and possibly for on-line diagnostics.

### References

- 1 B. O. Kolbesen and H. Strunk, *Inst. Phys. Conf. Ser.* **57**, 21 (1981).
- 2 A. Hanada, T. Furusawa, N. Saito, and E. Takeda, *IEEE Trans. Electron Devices* **38**, 895 (1991).
- 3 A. Hanada, T. Furusawa, N. Saito, and E. Takeda, *Semicond. Sci. Technol.* **7**, 593 (1992).

- 4 I. D. Wolf, J. Vanhellemort, A. Romano-Rodriguez, H. Norstrom, and H.E. Maes, *J. Appl. Phys.* **71**, 898 (1992).
- 5 I. D. Wolf, H. Norstrom, and H. E. Maes, *J. Appl. Phys.* **74**, 4490 (1993).
- 6 P. Gans and J. B. Gill, *Appl. Spectrosc.* **31**, 451 (1977).
- 7 W. F. Maddams, *Appl. Spectrosc.* **34**, 245 (1980).
- 8 L. Antonov and S. Stoyanov, *Appl. Spectrosc.* **47**, 1030 (1993).
- 9 W. H. Press, S. A. Teukolsky, W. T. Vetterling, and B. P. Flannery, *Numerical Recipes in Fortran — The Art of Scientific Computing* (Cambridge University Press, Cambridge, 1992).
- 10 K. Kobayashi, Y. Inoue, T. Nishimura, M. Hirayama, Y. Akasaka, T. Kato, and S. Ibuki, *J. Electrochem. Soc.* **137**, 1987 (1990).
- 11 S. Perkowitz, *Optical Characterization of Semiconductors: Infrared, Raman, and Photoluminescence Spectroscopy* (Academic Press, London, 1993).
- 12 J. F. Morhage, G. Kanellis, and M. Balkansky, *Solid State Commun.* (1979).
- 13 K. Yamazaki, M. Yamada, K. Yamamoto, and K. Abe, *Jpn. J. Appl. Phys.* **23**, 681 (1984).
- 14 B. Efron, *Ann. Stat.* **7**, 7 (1979).
- 15 B. Efron, *The Jackknife, the Bootstrap and Other Resampling Plans* (Society for Industrial and Applied Mathematics, Philadelphia, 1982).
- 16 B. Efron and R. Tibshirani, *Stat. Sci.* **1**, 54 (1986).
- 17 R. W. Cunningham, *Comp. Phys.* **7**, 570 (1993).

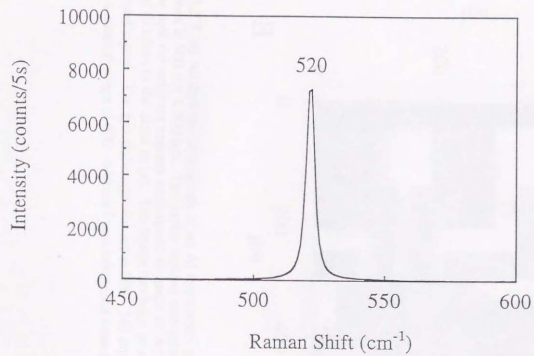


Figure 3.5.1. A typical Raman spectrum of a Si (001) wafer. The exposure time was 5 seconds, and the 514.5 nm line of a Ar<sup>+</sup> laser was used with a power of 100 mW.

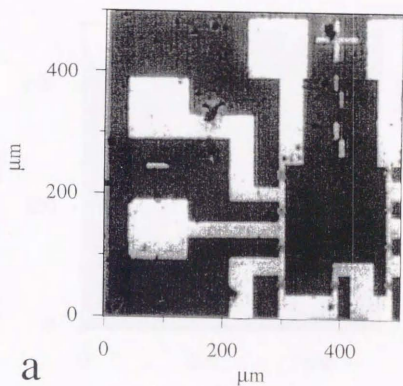
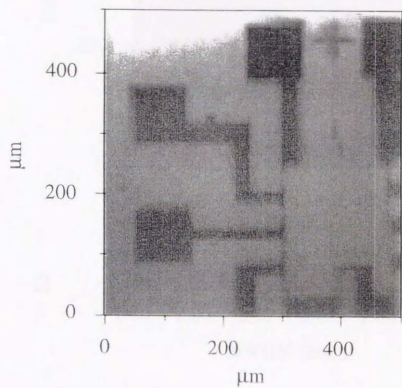
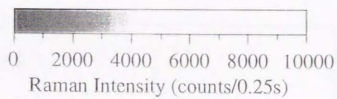


Figure 3.5.2. (a) An optical micrograph of an Al test circuit on a Si (001) wafer. The area shown is  $500\ \mu\text{m} \times 500\ \mu\text{m}$ . The darker regions correspond to areas of the bare Si substrate and the brighter regions correspond to areas of Al. (b) A Raman intensity image of Si taken in the same as (a). The image has been processed by subtracting the background signal. The spectral range was set at  $500 - 540\ \text{cm}^{-1}$ . A background image taken at a spectral range of  $600 - 640\ \text{cm}^{-1}$  was subtracted from this image.



**b**



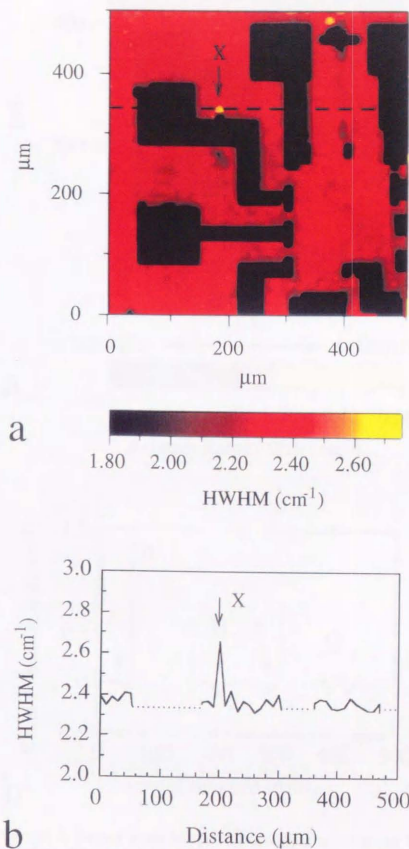


Figure 3.5.3. (a) An image of the variation in the HWHM of the Si Raman peak in the same area as Fig. 6.2a, and (b) a cross sectional profile. A very sharp peak is found in Fig. 6.3b at point X and corresponds to the damaged region in Fig. 6.2a.

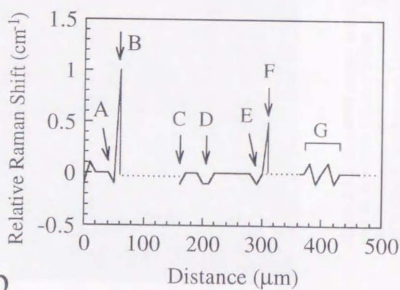
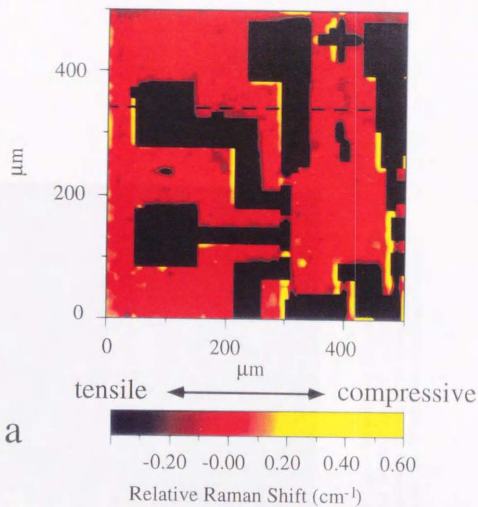


Figure 3.5.4. (a) A Raman strain image of the sample as indicated by the relative Raman shift of Si. The area of this image is same as the micrograph in Fig. 6.2a. The black regions corresponding to the brighter Al regions in Fig. 6.2a. Brighter areas represent areas with positive peak shifts and corresponds to compressive stress, while darker areas represent negative peak shifts and corresponds to tensile stress. (b) The cross sectional profile taken at the same location as Fig. 6.3b. A positive peak shifts at point B occurring at the left side edge of the Al circuit is clearly observed. Similar pairs of peaks are also observed on the wafer as indicated by points E and F.

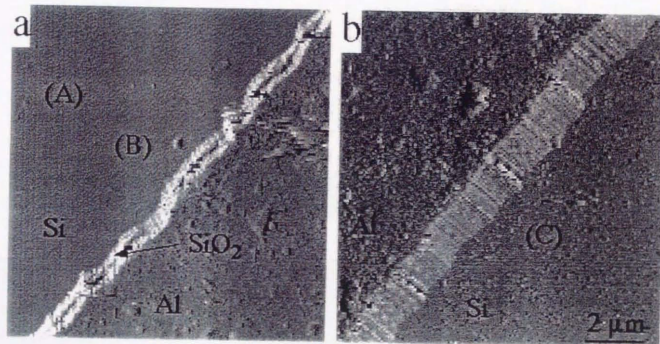


Figure 3.5.5. The AFM images at the boundary region between the deposited Al region and Si substrate (a) near points A and B and (b) near point C in Fig. 6.4b. Two deposited layers are found on the Si substrate as clearly shown in (a); however in (b), the SiO<sub>2</sub> layer is not observed. The images indicate that the Al layer was a misaligned toward the right by approximately 500 nm.

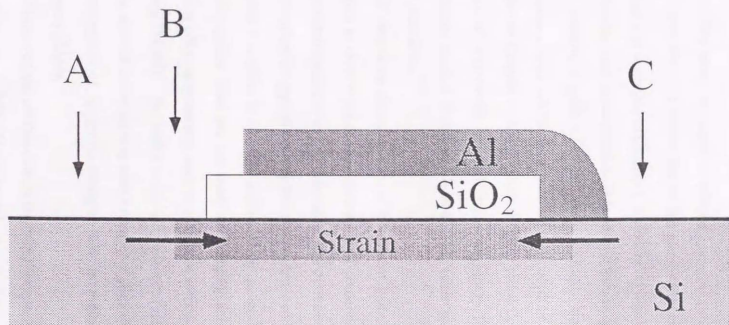


Figure 3.5.6. A schematic model for the observed Raman stress in the Al patterned circuit. The compressive stress at Point B was detected due to a slight error in masking for the Al. On the contrary the compressive stress left of point C was hidden by Al. The small tensile stress at point A and point C were caused by the reaction of the compressive stress.

## SUMMARY AND FURTHER MICRO-RAMAN SPECTROSCOPIC APPLICATIONS

In this study, the author developed a new micro-Raman system for the study of surface phenomena of semiconductor and metal oxide materials. This system has five advantages, as discussed in Chapter 1, including 1) high sensitivity, 2) Raman imaging, 3) electrochemical measurements, 4) combined Raman-photoelectrochemical imaging, and 5) imaging of peak width and peak position. Based on these advantages, the capabilities of this system have been demonstrated by four significant examples, as described in Chapter 3, i.e., 1) photochromic properties of  $\text{MoO}_3$  films, 2) imaging analysis of microscale crystallization of  $\text{MoO}_3$  films, 3) combined Raman-photoelectrochemical imaging analysis of  $\text{TiO}_2$  films, and 4) strain imaging analysis of  $\text{Si/SiO}_2$  interfaces.

Furthermore, the capabilities of this system, particularly in imaging analysis, can be applied to other types of characterization of semiconductors, e.g., ion implantation damage, determination of crystal orientation, and the measurement of free carrier density. This system can be applied not only for semiconductor and metal oxide materials but also for organic thin films or adsorbed molecules. In general, however, the Raman signals for such organic films are too small for imaging analysis, and thus some signal-enhancing effect is necessary, such as resonance effects and surface-enhanced Raman scattering (SERS). The author is studying adsorbed molecules using SERS imaging analysis, and this technique may have a number of potential applications, for example, in the examination of Langmuir-Blodgett (LB) monolayer films and self-assembled monolayers (SAM).

Moreover, the combination of the micro-Raman system and near-field scanning optical microscopy (NSOM) can provide even higher spatial resolution. NSOM has

attracted considerable interest as an instrument for imaging topographic and surface relief details of optical samples, with spatial resolution below the diffraction limit. Lateral resolutions of  $\lambda/20$  and vertical resolutions of  $\lambda/100$  have been claimed as achievable from the various NSOM systems. This is achieved in practice by scanning a miniature light-collection or light-emission aperture of suboptical wavelength dimensions over the sample surface. Tsai et al.<sup>1</sup> reported that Raman *spectra* of a diamond sample were recorded with subwavelength spatial resolution using a tapered-fiber optical probe in conjunction with a conventional Raman spectrometer. The author hopes that a combined high-sensitivity Raman spectrometer-NSOM system will provide Raman *images* with subwavelength spatial resolution.

## References

1. Tsai, D. P.; Othonons, A.; Moskovits, M.; Uttamchandani, D. *Appl. Phys. Lett.* **1994**, *64*, 1768.

## PUBLICATION LIST

### A. Original Papers

1. K. Ajito, L. A. Nagahara, D. A. Tryk, K. Hashimoto, and A. Fujishima,  
"A study of the photochromic properties of amorphous MoO<sub>3</sub> films using Raman  
microscopy."  
J. Phys. Chem., in press.  
(Section 3.2 of Chapter 3)
2. K. Ajito, D. A. Tryk, K. Hashimoto, and A. Fujishima,  
"Direct evidence for a reversible structural change in an amorphous material:  
Photochromic coloring and electrochromic decoloring of amorphous  
molybdenum oxide thin films," in preparation.  
(Section 3.2 of Chapter 3)
3. A. Fujishima, L. A. Nagahara, H. Yoshiki, K. Ajito, and K. Hashimoto,  
"Thin semiconductor films: photoeffects and new applications,"  
Electrochim. Acta **39**, 1229-1236 (1994).  
(Section 3.3 of Chapter 3)
4. K. Ajito, J. P. H. Sukamto, L. A. Nagahara, K. Hashimoto, and A. Fujishima,  
"Combined Raman and photoelectrochemical imaging system.  
Application to TiO<sub>2</sub> films grown anodically on Ti-Ag alloy,"  
J. Electroanal. Chem. **386**, 229 -233 (1995).  
(Section 3.4 of Chapter 3)

5. K. Ajito, J. P. H. Sukamto, L. A. Nagahara, K. Hashimoto, and A. Fujishima,  
"Strain imaging analysis of Si using Raman microscopy,"

J. Vac. Sci. Technol. A **13**, 1234-1238 (1995).

(Section 3.5 of Chapter 3)

6. K. Ajito, H. Hagiwara, D. A. Tryk, K. Hashimoto, and A. Fujishima,

"Two-dimensional SERS imaging of photoelectrochemically patterned  
azobenzene-LB film," in preparation.

(Chapter 4)

#### **B. Proceedings**

1. K. Ajito, J. P. H. Sukamto, K. Hashimoto, and A. Fujishima,

"Comparison of Raman and photocurrent mapping of oxide thin film electrode,"  
in *Proceedings of The First Korea-Japan Joint Seminar on Electrochemistry*,

Seoul (1993), p. 167-170.

## PRESENTATION LIST

### International

1. K. Ajito, J. P. H. Sukamto, K. Hashimoto, and A. Fujishima,  
"Comparison of Raman and photocurrent mapping of oxide thin film electrode,"  
The First Korea-Japan Joint Seminar on Electrochemistry,  
November 22-24, Hoam Hall, Seoul National University, Seoul, Korea (1993).
2. K. Ajito, J. P. H. Sukamto, K. Hashimoto, and A. Fujishima,  
"Mapping of bulk and surface electronic properties of thin semiconductor films.  
Application of a photo-current (-voltage) and Raman imaging system,"  
The Second International Symposium on New Trends in Photoelectrochemistry,  
March 22-24, Sanjo Kaikan, The University of Tokyo, Tokyo, Japan (1994).
3. K. Ajito, J. P. H. Sukamto, L. A. Nagahara, K. Hashimoto, and A. Fujishima,  
"Strain imaging analysis using Raman Microscopy,"  
American Vacuum Society 41st National Symposium,  
October 24-28, Colorado Convention Center, Denver, Colorado, USA (1994).

## ACKNOWLEDGMENTS

All the studies presented in this thesis have been carried out in the laboratory of Prof. Akira Fujishima, in the Department of Applied Chemistry, The University of Tokyo, from October in 1992 to September 1995. The completion of this thesis was only possible with the assistance of many people. First of all, I wish to express my deepest gratitude to Professor Akira Fujishima for his invaluable guidance and constant encouragement throughout my research program. I am greatly indebted to Prof. Kazuhito Hashimoto his invaluable suggestions, continuous encouragement, and careful reading of manuscripts. I would also like to thank Prof. Makoto Misono, Prof. Koichi Kitazawa, and Prof. Tadashi Watanabe for their valuable comments and advices. I am deeply grateful to Dr. Larry Nagahara, Dr. John P. H. Sukamto, Dr. Donald A. Tryk, Dr. Lei Jiang, Dr. Jian N. Yao, Dr. Xiao. M. Yang, Dr. Ryo Baba, and Dr. Tetsuya Miwa for their helpful discussions and eager collaboration. Great acknowledgment is also made to Ms. Yoko Takahashi, Ms. Kaori Seko, Ms. Yumica Suzuki, and Ms. Aomi Fujii for their constant help in official matters associated with laboratory life.

Several of the results described in this thesis could only have been obtained through collaborations with other research groups. I would like to thank Dr. T. Ogawa and Mr. T. Saito of Takenaka Technical Co., Research & Development Institute, for providing samples of anodic TiO<sub>2</sub> films and Prof. U. Nagashima of The University of Ochanomizu for helpful discussions on the Monte Carlo calculations.

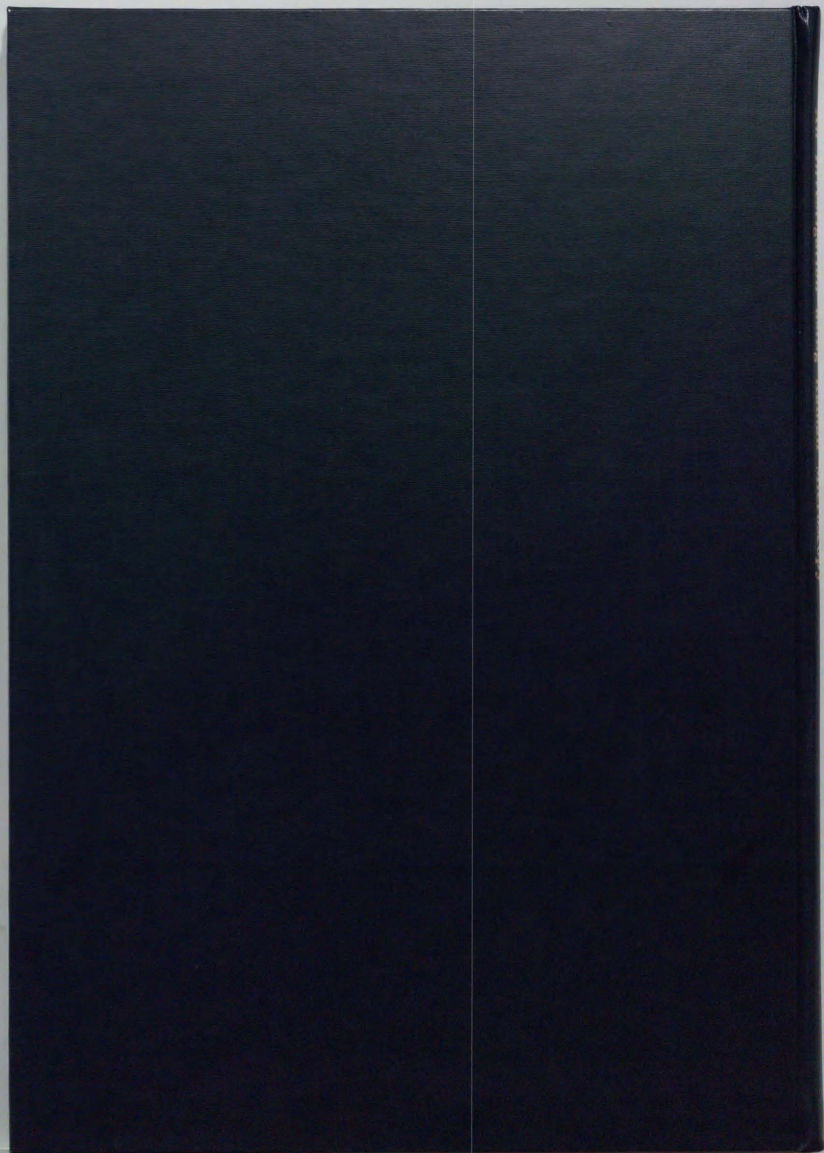
I wish to express my sincere gratitude to Prof. Masatoki Ito and Dr. Machiko Takahashi (University of Keio), for their useful discussions and kind instruction in various experimental techniques. It is my pleasure to express appreciation for my family, Chika Ajito (my wife), Satoshi Ajito (my son), Kenji Ajito (my father), Toyoko Ajito (my mother), Koji Ajito (my brother), Yuko Ajito, Yuki Ajito, Morio Tanaka, Toshiko Tanaka, Tomohiko Tanaka, and Machi Tanaka, for encouraging me continuously in my studies.

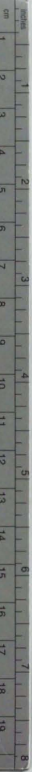
Finally, I wish to thank to all of the friends in Fujishima Laboratory, including Mr. Hajime Yoshiki , Dr. Hideki Sakai, Dr. Tomonori Saeki, Ms. Rong Wang, Mr. Takashi Yano, and Mr. Toshihiro Minabe for their continuous understanding and encouragement. I cannot write down the names of all the friend here, but I believe that I could not complete my dissertation without their kind assistance.

September 1995

味戸克裕

Katsuhiro Ajito





# Kodak Color Control Patches

© Kodak, 2007 TM Kodak

Blue	Cyan	Green	Yellow	Red	Magenta	White	3/Color	Black
[Patch 1]	[Patch 2]	[Patch 3]	[Patch 4]	[Patch 5]	[Patch 6]	[Patch 7]	[Patch 8]	[Patch 9]

# Kodak Gray Scale



© Kodak, 2007 TM Kodak

**A** 1 2 3 4 5 6 **M** 8 9 10 11 12 13 14 15 **B** 17 18 19

